

**THEORY AND EXPERIMENT ON THIN LIFES AT LOW  
REYNOLDS NUMBER**

by

Charles W. Wolgemuth

A Dissertation Submitted to the Faculty of the  
DEPARTMENT OF PHYSICS  
In Partial Fulfillment of the Requirements  
For the Degree of  
DOCTOR OF PHILOSOPHY  
In the Graduate College  
THE UNIVERSITY OF ARIZONA

2 0 0 0

THEORY AND EXPERIMENT ON THIN LIFE AT  
LOW REYNOLDS NUMBER

Charles W. Wolgemuth, Ph. D.  
The University of Arizona, 2000

Director: Raymond E. Goldstein

Many interesting problems in cellular biophysics involve the dynamics of filamentary elastic objects with bend and twist degrees of freedom, moving in a viscous environment. Motivated by the mysterious macrofiber formation in *B. subtilis* and the rotational dynamics of bacterial flagella, we have sought to establish a general theoretical structure to deal with elastic filament dynamics, analyze these equations for model systems, and to determine the important physical parameters that set the dynamical scales for these systems.

We first studied the novel problem of a rotationally forced elastic filament in a viscous fluid [1] to examine the competition between twist injection, twist diffusion, and writhing motions. Two dynamical regimes separated by a Hopf bifurcation were discovered: (i) diffusion-dominated axial rotation, or *twirling*, and (ii) steady-state crankshafting motion, or *whirling*.

Next, we extended elasticity theory of filaments to encompass systems, such as bacterial flagella, that display competition between two helical structures of opposite chirality [2]. A general, fully intrinsic formulation of the dynamics of bend and twist degrees of freedom was developed using the natural frame of space curves, spanning from the inviscid limit to the viscously-overdamped regime applicable to cellular biology.

To be able to measure the elastic properties of cell-sized objects, such as bacterial fibers [3], we utilized an optical trapping system to study the relaxation of a single fiber

of *B. subtilis* which was bent and then released. By analyzing the relaxation time, the bending modulus of the bacterial cell wall was measured to be  $1.6 \pm 0.6 \times 10^{-12}$  erg·cm. This number is important in understanding the scales of forces and torques that are present in macrofiber formation and motion, lending insight into the mechanism behind these phenomena.

## STATEMENT BY AUTHOR

This dissertation has been submitted in partial fulfillment of requirements for an advanced degree at The University of Arizona and is deposited in the University Library to be made available to borrowers under rules of the Library.

Brief quotations from this dissertation are allowable without special permission, provided that accurate acknowledgment of source is made. Requests for permission for extended quotation from or reproduction of this manuscript in whole or in part may be granted by the head of the major department or the Dean of the Graduate College when in his or her judgment the proposed use of the material is in the interests of scholarship. In all other instances, however, permission must be obtained from the author.

SIGNED: \_\_\_\_\_

## ACKNOWLEDGEMENTS

I would like to thank a number of people whose guidance, support, and friendship have not only made this possible, but also enjoyable [94].

I would first like to thank the scientists that I have collaborated with, and without whom I would definitely not have reached this point. Tom Powers analytical calculations, help, guidance and insight on the “Twirling and Whirling” paper transformed the results from merely interesting into something with much more depth and applicability. Tom is one of the finest physicists I have met and who has proven to me that it is much better to be excessively careful with a calculation the first time rather than trying to guess your way to the right answer. I wish him great luck at his new position and know that his physical intuition and care will grant him success. In the world of interdisciplinary science the greatest need is to find scientists who have the desire to cross boundaries and put forth the effort to communicate and learn new ways to explore their discipline. Neil Mendelson is one such scientist. His willingness to find out what physics could bring to the work he has been doing has been a great incentive for me to test out new areas. On top of that, he is also a wonderful biologist who provided great experiments that could be analyzed using physics while maintaining biological relevance and significance. Undergraduate research training is a great way for undergraduate students to learn what real science is about. On top of that, it gives graduate students a pseudo-advisor role. Joelle Sarlls has been a wonderful assistant in the lab and without her help the laser tweezer project would never have been finished. Good luck in graduate school, Joelle. Without the discussions and mathematical assistance of Greg Huber and Alain Goriely, the “Bistable Helices” paper could never have come together. This paper was truly a joint effort and showed how quickly a group of good scientists, coupled with a great idea, could accomplish a meaningful result.

My list of collaborators would not be complete without a special thanks to my advisor and friend, Ray Goldstein. Though not always the easiest person to track down, Ray taught me the techniques that will hopefully guide me through a life of good science. The life of a theorist can sometimes become overwhelmed with mathematics. This is not a bad thing, unless one loses sight of the physics. Ray always demanded me to step back from the calculation and explain the mathematical result physically. This is how intuition is gained. On top of this, Ray showed me that the most important questions to ask are not the most popular or the most fundable, but rather a good scientist should ask the questions that he finds most interesting. Interesting questions can lead to importance as easily as importance can instill interest. Thank you Ray for the help and guidance you have provided me.

## DEDICATION

This work is dedicated to my late father, Larry G. Wolgemuth.

## TABLE OF CONTENTS

List of Figures . . . . .	8
Abstract . . . . .	10
Chapter 1: Introduction . . . . .	11
1.1 Elastohydrodynamics . . . . .	11
1.2 Two Model Biological Elastic Filaments . . . . .	15
1.2.1 <i>B. subtilis</i> Macrofibers . . . . .	15
1.2.2 Bacterial Flagella . . . . .	21
Chapter 2: Twirling and Whirling: Viscous Dynamics of Rotating Filaments <sup>1</sup> . . .	25
2.1 Statement of the Problem . . . . .	25
2.2 Dimensional Analysis . . . . .	27
2.3 Linearized Dynamics . . . . .	30
2.4 Weakly Nonlinear Theory . . . . .	32
2.5 Swimming . . . . .	33
Chapter 3: Bistable Helices <sup>2</sup> . . . . .	35
3.1 Bacterial Flagellar Flipping . . . . .	35
Chapter 4: Experiments on <i>B. subtilis</i> Fibers <sup>3</sup> . . . . .	44
4.1 Basics . . . . .	44
4.2 Chiral Self-Propulsion on a Solid Surface . . . . .	45
4.3 Measurement of the Bending Modulus for <i>B. subtilis</i> . . . . .	49
Chapter 5: Conclusions . . . . .	53

---

<sup>1</sup>A modified version of the work that was previously published as [1].

<sup>2</sup>A modified version of the work that was previously published as [2].

<sup>3</sup>A modified version of the work that was previously published as [3].

Appendix A: Variations in $\vec{\Omega}$ and the basis vectors . . . . .	56
Appendix B: Derivation of the extrinsic force and writhing terms . . . . .	57
Appendix C: Linear Analysis of the Twirl-to-Whirl Instability . . . . .	59
Appendix D: Numerical Methods for Twirling and Whirling . . . . .	61
Appendix E: $\Psi$ to Real Space Conversion . . . . .	64
Appendix F: Growth Induced Buckling . . . . .	66
Appendix G: Derivation of the Dynamic Equations for $\Psi$ and $\Omega$ . . . . .	68
Appendix H: Correction to the Block Angle . . . . .	71
Appendix I: Bistable Parameters - From Hotani's data . . . . .	76
Appendix J: Stretching a Bistable Helix . . . . .	77
Appendix K: Fiber Dynamics with an Attached Bead . . . . .	80
References . . . . .	82



## LIST OF FIGURES

1.1	Diagrammatic representation of Stokes' problem I (SI) where a semi-infinite fluid is bounded by a wall that is moved impulsively, and Stokes' problem II (SII) where the wall is oscillated. . . . .	13
1.2	Diagrammatic representation of EHDI where an elastic filament in a viscous fluid is allowed to relax from a stressed state and EHDII where one end of the filament is oscillated [12]. . . . .	14
1.3	Stages in the growth and development of a bacterial macrofiber. . . . .	17
2.1	An elastic filament, rotated about $z$ at the left end, surrounded by a fluid of viscosity $\eta$ . . . . .	27
2.2	(a) Stroboscopic montage of the "whirling" filament, viewed from along the $z$ -axis, as it rotates clockwise; (b) side view at two times. . . . .	31
2.3	(a) Growth rates for the first three modes of the linear equation. Mode becomes unstable when the growth rate is positive. (b) Whirling frequencies for the first three modes. . . . .	32
2.4	(a) Amplitude $R$ (with a square root fit) and (b) crankshafting frequency of filament tip motion as a function of frequency offset from primary instability. (c) and (d); filament shapes for $(\omega - \omega_c)/\omega_c = 0.27$ and $3.52$ , with $\Gamma = 1$ . . . . .	33
2.5	Propulsive force generated by steady-state whirling motions, as a function of driving frequency. . . . .	34
3.1	Bistable helices. (a) Flagella of <i>Salmonella</i> , with coexisting left- and right-handed helices (arrows), courtes of H. Hotani. (b) Solenoidal form of <i>B. subtilis</i> fiber, with coexisting helices, courtesy of M. Tilby. . . . .	37
3.2	Description of bistable helices. (a) The double-well potential in the twist variable, (b) a helix corresponding to (c) the elementary front solution of the twist. . . . .	40

3.3	Geometry for the relation $\theta_+ + \alpha - \theta_- = \pi$ . Rectangles are unit cells of the concatenated helices, with radii $R_{\pm}$ , pitches $p_{\pm}$ , and tangents $\mathbf{t}_{\pm}$ . . .	40
3.4	Front propagation along a helix. Two possible modes are (A) crankshafting and (B) speedometer-cabbling. . . . .	42
4.1	Images of macrofibers from top and side within a glass growth chamber. Scale bar is 0.5 mm. . . . .	46
4.2	Rolling sequence. Dual-view images showing motion of a macrofiber. Panels are at times (b) 28 s., (c) 80 s., and (d) 128 seconds after (a). Scale bar is 0.5 mm. . . . .	47
4.3	Pivoting and fiber growth. (a) uniform rotational motion of left (squares) and right-handed (circles) fibers, and (b) their length evolution, showing several folding events for the RH case. (c) symmetry argument for angular direction of pivoting, with $\mathbf{n}$ the surface normal, $\mathbf{h}$ the helicity vectors (lying in the plane, along the plectoneme axis), and $\mathbf{p}$ the resultant pivoting forces, also in the plane. (d) composite image from above showing pivoting around $\mathbf{n}$ . . . . .	49
4.4	Schematic of the setup of the optical trapping system. Note: diagram is not drawn to scale. . . . .	50
4.5	Exponential relaxation of a bead attached to a fiber tip, following displacement by an optical trap. Inset shows a $2 \mu\text{m}$ bead attached to a filament. . . . .	51
H.1	(a) Numerical and Analytic results for the deviation in the block angle due to a finite width front. (b) shows the deviation that occurs at large $\xi$ . Figure courtesy of A. Goriely. . . . .	75
K.1	Variation in $k_1 L$ , where $k_1$ is the wavenumber of the first mode, with $\epsilon$ . . . . .	81

## ABSTRACT

Many interesting problems in cellular biophysics involve the dynamics of filamentary elastic objects with bend and twist degrees of freedom, moving in a viscous environment. Motivated by the mysterious macrofiber formation in *B. subtilis* and the rotational dynamics of bacterial flagella, we have sought to establish a general theoretical structure to deal with elastic filament dynamics, analyze these equations for model systems, and to determine the important physical parameters that set the dynamical scales for these systems.

We first studied the novel problem of a rotationally forced elastic filament in a viscous fluid [1] to examine the competition between twist injection, twist diffusion, and writhing motions. Two dynamical regimes separated by a Hopf bifurcation were discovered: (i) diffusion-dominated axial rotation, or *twirling*, and (ii) steady-state crankshafting motion, or *whirling*.

Next, we extended elasticity theory of filaments to encompass systems, such as bacterial flagella, that display competition between two helical structures of opposite chirality [2]. A general, fully intrinsic formulation of the dynamics of bend and twist degrees of freedom was developed using the natural frame of space curves, spanning from the inviscid limit to the viscously-overdamped regime applicable to cellular biology.

To be able to measure the elastic properties of cell-sized objects, such as bacterial fibers [3], we utilized an optical trapping system to study the relaxation of a single fiber of *B. subtilis* which was bent and then released. By analyzing the relaxation time, the bending modulus of the bacterial cell wall was measured to be  $1.6 \pm 0.6 \times 10^{-12}$  erg·cm. This number is important in understanding the scales of forces and torques that are present in macrofiber formation and motion, lending insight into the mechanism behind these phenomena.

# Chapter 1

## Introduction

Over three and a half billion seconds ago, Kirchhoff presented the fundamental equations for elastic rods, the basis for most subsequent theory on the statics and dynamics of elastic filaments [4]. For at least as many *years*, terrestrial life forms have been engineering and generating all manner of elastic rods, one of the key structural elements of single and multicellular life. It is likely, therefore, that biology has much to teach us about the rich phenomena and inherent possibilities contained within the basic framework of elasticity theory.

Filamentary objects are ubiquitous in the world of cellular biology. From DNA to microtubules, actin to bacterial macrofibers, filamentous structures perform a wide variety of tasks and are present at all length scales. In biology, deformations of these filaments usually lead to interesting phenomena, such as morphological changes in DNA during transcription or replication [5, 6, 7] or chirality flipping in bacterial flagella [8, 9, 10, 11]. Most of these deformations involve bending in which the length scale of the deformation is much larger than the radius of the filament. Under these circumstances, it is reasonable to treat these filaments as elastic objects. Since the biological filaments that we will be concerned with are all found in fluids, namely water, the elastic dynamics of the filaments must be coupled to the hydrodynamics of the fluid. This gives rise to a field of study called *elastohydrodynamics* [12].

### 1.1 Elastohydrodynamics

To understand the dynamics of elastic objects in a viscous environment it is first necessary to understand how to couple elasticity with fluid dynamics. The basic equation of hydrodynamics is the Navier-Stokes (N-S) equation.

$$\rho(\partial_t \mathbf{u} + (\mathbf{u} \cdot \nabla) \mathbf{u}) = -\nabla P + \eta \nabla^2 \mathbf{u} \quad (1.1)$$

with  $\rho$  the mass density of the fluid,  $\mathbf{u}$  the velocity,  $P$  the pressure, and  $\eta$  the viscosity of the fluid. This equation balances the acceleration of the fluid with the forces that are present and, through the viscosity term, also accounts for the stress that the fluid exerts on itself when fluid layers slide past one another. By scaling out the dimensions of this equation by choosing  $\tilde{\mathbf{u}} = \mathbf{u}/v$ ,  $\tilde{\mathbf{x}} = \mathbf{x}/L$ ,  $\tilde{t} = tL/v$ , and  $\tilde{P} = PL/\eta v$ , this equation can be shown to depend on one parameter, the Reynolds number,  $Re = vL/\eta$ , as

$$Re (\partial_t \mathbf{u} + (\mathbf{u} \cdot \nabla) \mathbf{u}) = -\nabla P + \nabla^2 \mathbf{u} \quad (1.2)$$

where the tildes have been dropped for simplicity. The Reynolds number is a ratio between the inertial and viscous forces in the fluid. When  $Re \gg 1$ , inertial effects dominate. When  $Re \ll 1$ , viscous forces prevail. Since the Reynolds number is length dependent, hydrodynamics is very different for small and large sized objects. For microscopic objects, the viscosity of the fluid in which they live is so dominant that inertial effects can be ignored. A swimming bacterium like *E. coli* in water has a length scale of  $10^{-4}$  cm, swims with a velocity of  $10^{-3}$  cm/s, and water's viscosity is  $10^{-2}$  Poise. This gives a Reynolds number of  $10^{-5}$ , a realm where inertia is completely absent.

To better understand the effects of the viscous term in the N-S equation, Stokes [13] posed two ideal problems to study these effects. These problems assumed a semi-infinite fluid bounded by a wall (See Fig. 1.1). In Stokes first problem, SI, the wall is moved impulsively at time  $t = 0$ . For Stokes second problem, SII, the wall is oscillated at a frequency,  $\omega$ . For both of these problems the velocity profile for the fluid is calculated. The velocity is assumed to be of the form  $\mathbf{u} = u(x, t)\hat{\mathbf{y}}$ . Under this assumption, the nonlinear advective piece of the N-S equation is zero and the equation simplifies to

$$u_t(x, t) = \nu u_{xx}(x, t) \quad (1.3)$$

where  $\nu = \eta/\rho$  is the kinematic viscosity. The pressure term has been neglected due to the fact that a constant pressure is a solution to the equations and it can be shown that variations in the pressure will diffuse away at the speed of sound, which for an incompressible fluid is infinitely fast. This equation is the diffusion equation where one time derivative is balanced by two spatial derivatives. In both of Stokes problems, the boundary conditions are assumed to be a no-slip condition at the wall and that the velocity at infinity is zero. The fundamental feature of SI is that there is not a characteristic length

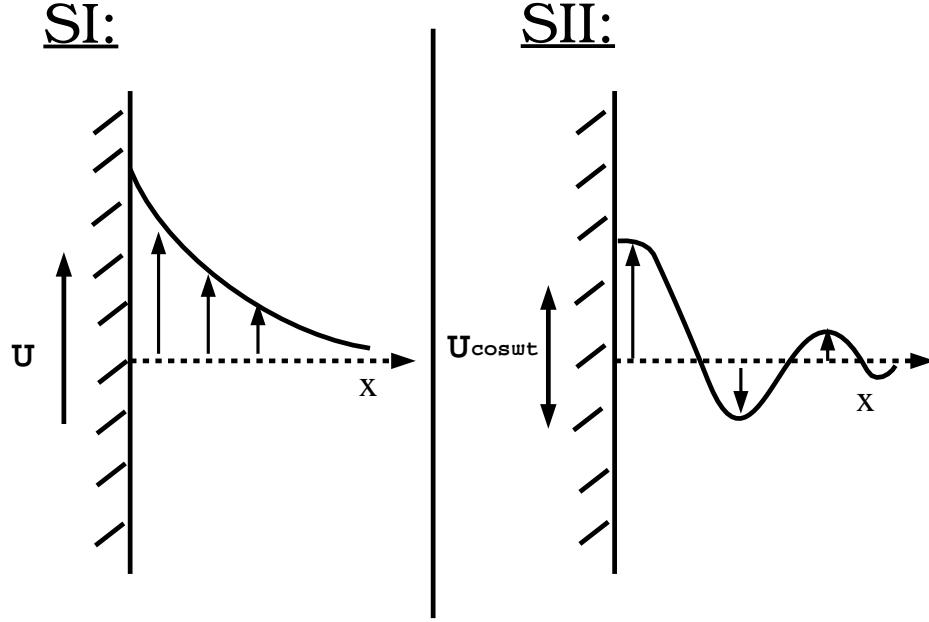


Figure 1.1: Diagrammatic representation of Stokes' problem I (SI) where a semi-infinite fluid is bounded by a wall that is moved impulsively, and Stokes' problem II (SII) where the wall is oscillated.

scale that is defined by the parameters of the problem. Therefore, the velocity at any point  $x$  and time  $t$  depends on the ratio  $x/(\nu t)^{1/2}$ . In SII, a characteristic length scale can be created as  $\ell_S(\omega) = (\nu/\omega)^{1/2}$ . This determines the length over which oscillations in the velocity profile will decay.

An elastic filament can be parameterized by the distance along its central axis,  $s$ , the arc length. If the position of the centerline is given by  $\mathbf{r}(s)$ , the energy cost for deforming the filament from its unstressed state can be written as:

$$\mathcal{E} = \int_0^L \kappa^2 ds \quad (1.4)$$

where  $\kappa^2 = \mathbf{r}_{ss} \cdot \mathbf{r}_{ss}$  is the curvature of the filament, and  $A$  is the material dependent bending modulus. The elastic force per length,  $\mathbf{f}$ , that acts on the filament is found from this energy functional by  $\mathbf{f} = -\partial\mathcal{E}/\partial\mathbf{r}$ . Taking this functional derivative leads to a force per length,

$$\mathbf{f} = -A \left( \mathbf{r}_{4s} + \frac{3}{2} \partial_s ((\mathbf{r}_{ss} \cdot \mathbf{r}_{ss}) \mathbf{r}_s) \right) \quad (1.5)$$

This elastic force can be coupled to the low Reynolds number hydrodynamics of the surrounding fluid by assuming that the filament is long and thin. Through this method

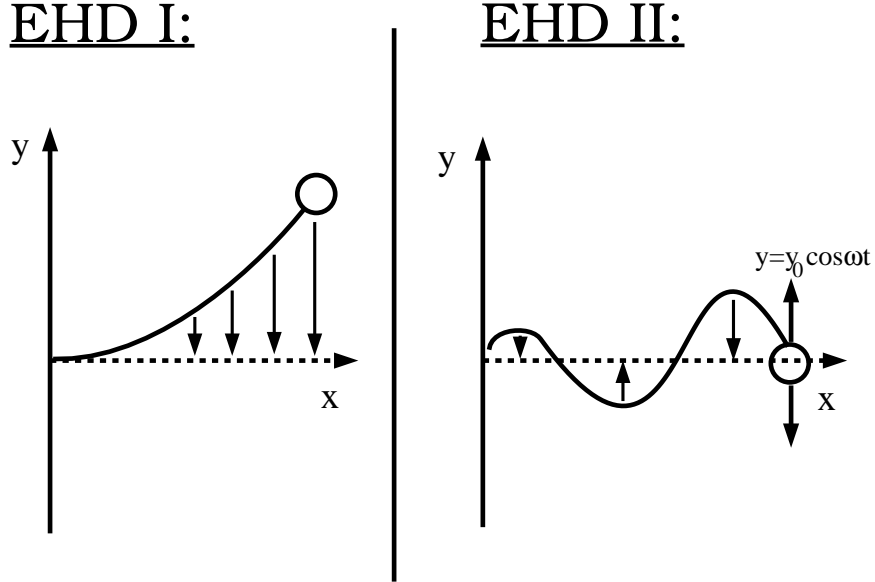


Figure 1.2: Diagrammatic representation of EHD I where an elastic filament in a viscous fluid is allowed to relax from a stressed state and EHD II where one end of the filament is oscillated [12].

of matched asymptotics, called *slender-body hydrodynamics* [14], the force is found to be proportional to the fluid drag by

$$\zeta_{\parallel} \hat{\mathbf{t}} \hat{\mathbf{t}} \cdot \mathbf{r}_t + \zeta_{\perp} (\mathbf{I} - \hat{\mathbf{t}} \hat{\mathbf{t}}) \cdot \mathbf{r}_t = \mathbf{f}. \quad (1.6)$$

where  $\zeta_{\perp} = 4\pi\eta/(\ln(L/2a) + c)$  is the drag coefficient for motion perpendicular to the long axis of the filament,  $\zeta_{\parallel} = \zeta_{\perp}/2$  is the drag coefficient for motions along the tangent vector,  $\mathbf{t} = \mathbf{r}_s$  is the tangent vector,  $L$  is the length of the filament,  $a$  is the radius, and  $c$  is a constant of order unity that depends on the shape of the body.

If we are interested in small deformations of an initially straight elastic filament, the leading order dynamic equation that couples elasticity to viscous fluid dynamics is

$$\zeta_{\perp} \mathbf{r}_t \approx -A \mathbf{r}_{4s}. \quad (1.7)$$

This equation looks and acts a lot like the diffusion equation. It is the balance of one time derivative and *four* spatial derivatives and is known as a *Hyperdiffusion* equation, with  $A/\zeta_{\perp} = \tilde{\nu}$  the hyperdiffusion constant.

By analogy to Stokes' Problems I and II, two similar problems can be defined for elasto-hydrodynamics (EHD) [12]. In EHD I, an initially straight filament is held at one

end, bent from the other end, and then allowed to relax to its unstressed state. The relaxation in this problem is exponential with a relaxation time of  $\tau = L^4/\tilde{\nu}k^4$ , where  $k$  is a wave number that depends on the boundary conditions. If one end is clamped ( $\mathbf{r}(0) = \mathbf{r}_s(0) = 0$ ) and the other end is free ( $\mathbf{r}_{ss}(L) = \mathbf{r}_{3s}(L) = 0$ ),  $k \approx 1.87$ . In EHD II, one end of a filament is oscillated while the other end is free to move. As in SI, there is a preferred length scale for this problem given by  $\ell(\omega) = (\tilde{\nu}/\omega)^{1/4}$ . Oscillations in the filament die out exponentially on this length scale much as they did in the strictly fluid dynamical problem. The power of 1/4 comes from the four spatial derivatives (as opposed to two in SII) and has been verified in experiment [12].

## 1.2 Two Model Biological Elastic Filaments

Biology has found many uses for elastic filaments. The most well known of these is DNA. However, due to its size, the dynamic behavior of DNA and some other biological filaments, such as actin, is dominated by thermal fluctuations. At a larger length scale, where thermal fluctuations can be ignored, filamentary objects are still abundant. The bacterial flagellum, a helical filament that is rotated to provide propulsion, and bacterial macrofibers are two systems whose dynamics can be understood through application of elasticity and low Reynolds number hydrodynamics. The Reynolds number for a rotating bacterial flagella is between  $10^{-5}$ – $10^{-3}$  and for the motions observed in *B. subtilis* macrofibers the range is  $10^{-4}$  –  $10^{-2}$ . Understanding the dynamics of these systems can shed light on important issues in biology, such as bacterial propulsion and the structure of cell wall peptidoglycan in gram positive bacteria, as well as being model systems to test and expand our knowledge of the physics of the coupling between elasticity and viscous hydrodynamics.

### 1.2.1 *B. subtilis* Macrofibers

*Bacillus subtilis* is a common gram positive bacterium. Individual cells are cylindrical in shape with a length of  $\sim 4\mu\text{m}$  and a diameter of  $\sim 0.7\mu\text{m}$ . Under certain mutations, cells become autolysin-deficient. Autolysin is responsible for cleaving the cell wall upon replication and allowing the parent and daughter cells to separate. In cells with these mutations, cells replicate but fail to separate. Since the cells always grow length-wise along the cylinder axis, growth of these mutant strains results in a long chain of inter-



Strain	Average Doubling Time (min)	Average Buckling Length ( $\mu\text{m}$ )
FJ7 right-handed	77.4	166.0
FJ7 left-handed	87.7	244.1
RHX left-handed	143.3	1,480.7
RHX right-handed	97.7	936.3

Table 1.1: Different Strains of *B. subtilis*. Data taken from [17].

connected cells, a bacterial fiber (See Fig. 1.3) [15]. Mendelson observed that growth occurs at all points along the fiber's length. This growth is exponential in time with a doubling time that varies from 63 to 193 minutes depending on the strain of mutant [16, 17]. It is observed that these fibers grow to a certain length (90 - 2,800  $\mu\text{m}$ ) and then they buckle and wrap around themselves like an overtwisted phone cord (See Fig. 1.3), a shape known as a plectoneme. As this folded fiber continues to grow, it reaches a new length at which it will once again buckle and wrap itself into a supercoiled plectoneme, or macrofiber. The handedness of this secondary plectoneme is the same as the original handedness of the first structure. For any fiber of the same strain, grown in the same culture, all helical elements will be of the same handedness, and each folding cycle maintains the initial helix hand [16]. As well, it has been shown that the number of wrappings per length and the rate of turning of fibers as a function of their elongation is a constant for all stages of macrofiber growth. This process continues up until a point where the macrofiber is too stiff to fold anymore, after tens of folding cycles. At this point, the macrofiber assumes a ball-like structure. Though the plectonemic structure is the most common, under some growth conditions with certain strains of fibers, a helical, or solenoidal, shape is undertaken [18].

The handedness of these plectonemic structures depend on a great many factors, such as the strain that is used, the temperature of the surrounding fluid, pH, and the presence of salts in the growth medium.

*Temperature:* The first factor that affects the macrofiber torsion is the temperature [19]. In FJ7 strains, increasing the temperature was shown to transform right-handed fibers into left-handed fibers. This variation in torsion is roughly linear in the temperature.

*Lysozyme and Autolysin:* Addition of lysozyme or crude autolysin to the growth media

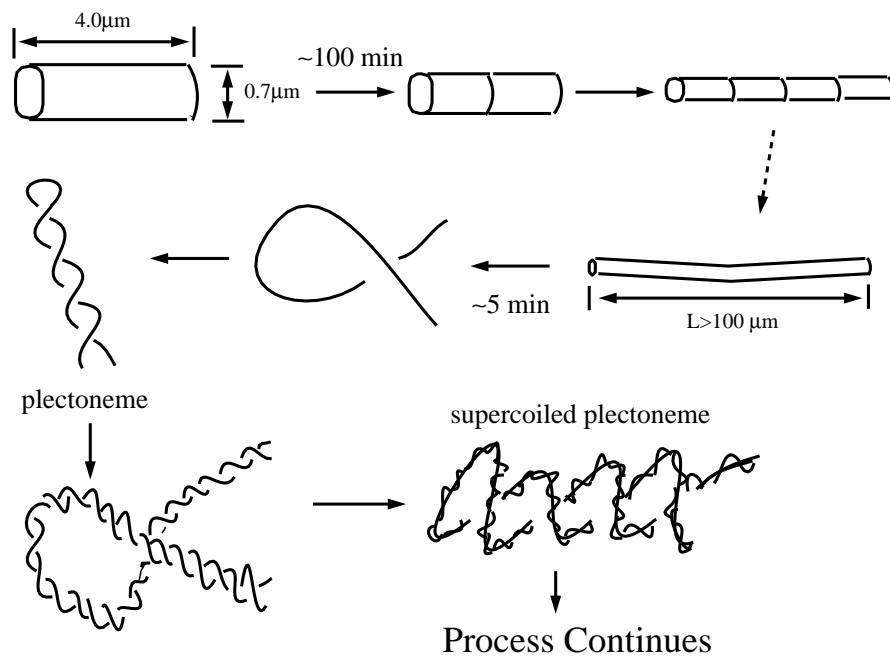


Figure 1.3: Stages in the growth and development of a bacterial macrofiber.

causes live helical macrofibers to undergo specific “relaxation” motions [19]. Lysozyme is an enzyme that breaks the glycan chains, or backbone, in peptidoglycan (the major component in bacterial cell walls). After these chains are broken, the cell effectively has no cell wall and at this point is called a protoplast. When lysozyme is added to the growth medium, the peptidoglycan chains begin to be cleaved, causing motions where the fibers always initially turn in a right-handed fashion. This is independent of the initial handedness of the fibers. Therefore, left-handed fibers tend to unwind and right-handed fibers tend to tighten up. Usually left-handed structures dissolve before becoming completely unwound, but there are occasionally fibers that go from a left-handed state into a right-handed state. In addition to just measuring the direction of turning of the fibers, the rate of turning and time for total breakdown of the structure have also been measured in the presence of lysozyme. It is observed that the rate of turning and breakdown time are both more rapid the more left-handed a fiber initially is. Relaxation motions appear not to be dependent on the medium in which the fiber is grown. But, if the fibers were exposed to either inactivated lysozyme or to polylysine, no relaxation motions were observed. This is evidence that supports that the relaxation motions are caused by cleavage of the peptidoglycan by lysozyme.

Right and left-handed macrofibers were also introduced into media containing crude autolysin at different pH. Two different series were examined, one with pH of 5.6 where the glucosaminidase, cleaving of the glycan chain, activity is favored and one at pH of 8.0 where the amidase activity is favored. Lysozyme relaxation motions were only induced in the pH of 5.6. At pH 5.6, no breakdown was observed. At pH 8.0, macrofiber breakdown was observed where the large structure broke down liberating lengths of cellular filaments that retained helical shape. Macrofibers of either hand incubated at either of these pH values, without autolysins or crude extract, did not display any of this behavior. This is evidence that the helical shape is maintained by the glycan backbone not by the short peptide cross-links of the peptidoglycan.

*Magnesium and Ammonium:* Bacterial cells cannot grow in the absence of magnesium or a nitrogen source such as ammonium. Magnesium plays a very important role in bacterial growth and stability of the shape of the cell. It is required for the integrity of the ribosome and membrane structure and also aids in peptidoglycan synthesis. As well, it also acts as cofactor in many biochemical reactions. Magnesium ions have been shown to

bind to peptidoglycan and teichoic acid, as well as influencing the susceptibility of cells to degradation by lysozyme.

Magnesium sulfate was added to different growth media with different strains of *B. Subtilis* [20]. In almost every case, addition of magnesium sulfate to the growth medium resulted in fibers twisting in a more right-handed way, and the amount of right-handedness increased with increased magnesium concentration. It was seen that in some fiber strains a twist inversion could be produced where the fibers would go from left to right-handed by adding magnesium sulfate. In other strains this inversion could not be produced.

Addition of ammonium sulfate to the growth medium causes the fibers to be more left-handed than they are when grown in the normal medium. The extent to which this has been seen is very qualitative but in all strains observed, ammonium sulfate caused the fibers to be more left-handed than normal. Of all the neutral salts that have been added to the medium, ammonium sulfate is the only one that has caused a left-handed shift in the fibers. By examination of a variety of salts, it has been determined that the cation is the part of the salt that affects twist development of the fibers.

*D-cycloserine and D-alanine:* In examining C6D fibers that normally grow left-handed [21], it has been seen that increasing the concentration of D-alanine in the growth medium causes fibers to grow more right-handed up until 15mM concentration is reached. After this point, with increased D-alanine concentrations, fibers grow more left-handed. D-alanine has also been shown to just produce more right-handedness in other strains of *B. Subtilis*. The second transition, where increased amounts of D-alanine produce more left-handedness, that was found in C6D has only been observed in two other strains, RHX 11S and 2C8.

Concentrations of D-cycloserine were examined on C6D fibers at different temperatures. It was seen that right-handed fibers were converted into left-handed structures by the addition of D-cycloserine. Left-handed C6D fibers were produced at 48 degrees Celsius and then D-cycloserine was added and no change in the twist state was observed. When left-handed fibers that were not as left-handed as those produced at 48 degrees Celsius were introduced to D-cycloserine, right-handed structures were produced. When FJ7 and A734 fibers were introduced to D-cycloserine, right-handed forms were converted to left-handed, whereas, left-handed structures were unaffected by the presence of D-cycloserine. When magnesium ions were added to the FJ7 medium so that the FJ7 fibers would be

at the same degree of twist as the A734 fibers, it was observed that the degree to which the FJ7 fibers twist changed due to D-cycloserine concentration was equivalent to that of the A734 fibers. It was also observed in other mutants that higher D-cycloserine concentrations cause more left-handedness of the fiber. When two left-handed mutants, PS5 and PS6 $\mu$ B, were introduced to D-cycloserine concentrations, their twist was unaffected by D-cycloserine. However, when right-handed mutants were exposed to D-cycloserine, their twist was affected to the left-hand side.

*Combinations of different factors:* It has been observed that many factors governing torsion of the bacterial fiber are additive [21]. This means that a change in the torsion towards the left-hand side can be produced by a factor such as D-cycloserine but this shift can then be reversed by addition of a factor that produces more right-handedness in that strain of fiber. Experiments were done with strains C6D and FJ7. With the C6D strains, different combinations of temperature, D-alanine, and D-cycloserine were used. It was noticed that temperature and D-cycloserine were left-hand factors, and that D-alanine was a right-hand factor. With the FJ7 strain, magnesium sulfate and ammonium sulfate were used as well as temperature, D-cycloserine and D-alanine. There was good evidence for this additive nature of the factors seen in both cases.

Through the addition of certain chemicals, such as lysozyme and autolysin, that only affect the cell wall chemistry, Mendelson has shown that the peptidoglycan structure in the cell wall is responsible for the supercoiling phenomena. The results reviewed here describe some very complex and interesting dynamical behaviors that are observed in these systems and appear to be mostly dependent on the elasticity of the cell wall material. However, the actual mechanism behind these motions is not well understood. Many models have been proposed that appeal to a growth induced twisting stress in the cell wall to account for the chiral conformations that are observed. However, since in some circumstances [19, 18] stable *single* filament helical structures are observed, a more complete elastic picture, involving preferred curvature and twist, may be required to describe these systems. Another possible mechanism driving the initial buckling could also be due to tension induced by drag on the growing ends of the fiber<sup>1</sup>. However, as of yet, no good working model has been able to correctly account for the dynamic behavior that is observed. It is hoped that through the study of the dynamics of this system a

---

<sup>1</sup>See Appendix F

greater insight into the structure of the cell wall can be attained. Also, this can lead to a better understanding of the forces and mechanisms behind bacterial shape and the relationship between growth and shape.

### 1.2.2 Bacterial Flagella

The bacterial flagellum is a helical filament that is rotated by a motor that is encased within the cell wall and powered by proton influx across the inner membrane providing a propulsive force to the cell. Some bacteria only possess one flagellum; while others, such as *E. coli*, have many flagella that are isotropically distributed over the cell body. The flagellum is made up primarily of 11 protofilaments of a single protein, flagellin. A typical flagellum from such bacteria as *E. coli* or *Salmonella* has a diameter of 23 nm and a length of up to 15  $\mu\text{m}$ . Normally, the pitch of the helix is around 2.3  $\mu\text{m}$  and the radius of the helix is about 0.2  $\mu\text{m}$  (corresponding to a curvature of 1.2  $\mu\text{m}^{-1}$  and a torsion of 2.1  $\mu\text{m}^{-1}$ ). Bacterial cells swim at speeds of 20-30  $\mu\text{m/s}$  along straight lines. In multiflagellated bacteria, the flagella bundle together as the bacterium swims. Every few seconds, the cell randomizes its direction by reversing the direction the flagellar motors turn. This reversal lasts for about a tenth of a second and causes the flagellar bundle to fly apart. When the motors return to their original direction, the bundle reforms and the cell goes off in a new direction. This process of swimming for a period of time and then randomizing orientation is called “run and tumble”. This allows for the bacterial cell to move about in the manner of a random walk and allows the cell to sample its environment.

Under static conditions, bacterial flagella are normally seen to exist in one state of chirality: they possess a given pitch and radius of curvature that is roughly constant along the length of the filament. Different species of bacteria produce flagella that have different chirality. However, only a few different morphologies have been observed in nature. Calladine proposed a microscopic model [22, 23] based on the packing of flagellin in the flagellar filament that predicts 12 conformational states for flagella. So far, only 7 of these have been observed in nature (the so-called normal, curly, curly I, curly II, coiled, semi-coiled, and straight states). It has been observed [24, 25] that when suitable ratios of flagellin from different species are copolymerized, that flagella consisting of two connected helices with different chirality are formed. These dual-chirality flagella

Conformation	Pitch ( $\mu\text{m}$ )	Radius ( $\mu\text{m}$ )	Curvature ( $\mu\text{m}^{-1}$ )	Torsion ( $\mu\text{m}^{-1}$ )
normal (L)	2.29	0.23	1.23	1.99
curly (R)	1.14	0.15	2.71	3.28
curly I (R)	0.93	0.16	3.33	3.08
curly II (R)	1.00	0.075	2.42	5.15
coiled (L)	0.69	0.76	1.29	0.19
semi-coiled (R)	1.24	0.26	2.44	1.85
straight	$\infty$	0	0	0

Table 1.2: Different Chiralities of Bacterial Flagella [11, 27]. (R) stands for right-handed and (L) left-handed.

are statically stable structures. Asakura [26] noticed that, by changing the pH or ionic strength of the solution, a normally coiled flagella could be caused to transform to a different helicity.

Dynamical transformations between states of opposite chirality have also been observed. MacNab and Ornston [8] took dark-field images of swimming *Salmonella* and discovered that under right-handed torsion, when the flagellar motor was operating in reverse, that the normally left-handed flagellar filament would flip to the right-handed “curly” state. This transition was observed to begin at the point where the flagellum attaches to the cell body and would then propagate distally, away from the end of the filament connected to the body. The transition region was observed to be small: the flagellar conformation was as if two helices of different pitch and radius were connected end to end. When the motor reversed again, the flagella also flipped back to the normal state. This type of behavior was also seen in *B. subtilis* and *E. coli* flagella. More recently, Berg [9] found that the flagella on bacteria that were swimming close to a glass surface would make a transition from either a right- or left-handed conformation to the straight state. This transition also occurred starting at the proximal end of the flagella and propagated distally. When the flagella moved far enough away from the glass surface, it was seen that a rapid ( $< 100$  ms) transition back to the original helical conformation propagated from the distal end of the filament proximally.

Hotani was able to induce similar transitions by flowing fluid past stationary flagella [11]. He removed flagella from *Salmonella* and found that one end would usually stick to a glass coverslip leaving the other end free. When fluid was flowed past these filaments, it was observed that its free portion would transform cyclically to a state of the opposite

handedness (curly or semi-coiled). Hotani noted three phases of this transition: initiation, growth, and travel. In the initiation and growth stages, a small portion of the flagella at the afixed end would transform to an opposite handed chirality and the rest of the flagellar filament would begin rotating. The region of opposite chirality would grow due to this rotation and the normal helicity region depleted. When the right-handed region had grown to a certain size, the point at the afixed end would flip back to the normal state. The right-handed region would then start rotating in the opposite direction and propagate down to the end of the filament and out, this being the travel stage. This process of initiation, growth, and travel would repeat.

Though a great deal of work has been done studying the static conformations of elastic filaments, little has been done to correctly model and analyze their three dimensional viscous dynamics. To understand the dynamical behavior of biological filaments, such as bacterial flagella and bacterial macrofibers, this type of analysis is required. This work seeks to establish a general theoretical structure to deal with elastic filament dynamics, analyze these equations for model systems, and to determine the important physical parameters that set the dynamical scales for these systems. In the second chapter, we study the novel problem of a rotationally forced elastic filament in a viscous fluid to examine the competition between twist injection, twist diffusion, and writhing motions. Two dynamical regimes separated by a Hopf bifurcation were discovered: (i) diffusion-dominated axial rotation, or *twirling*, and (ii) steady-state crankshafting motion, or *whirling*. This work was previously published in [1] and was done in collaboration with Thomas R. Powers and Raymond E. Goldstein. The third chapter extends elasticity theory of filaments to encompass systems, such as bacterial flagella, that display competition between two helical structures of opposite chirality. A general, fully intrinsic formulation of the dynamics of bend and twist degrees of freedom was developed using the natural frame of space curves, spanning from the inviscid limit to the viscously-overdamped regime applicable to cellular biology. This fourth chapter was previously published in [2] and was work done in collaboration with Raymond E. Goldstein, Alain Goriely, and Greg Huber. Finally, chapter four deals with the complex motions that are observed in growing *B. subtilis* macrofibers that are near a surface. The dynamics of these fibers can be used to estimate the forces and torques that are generated in the growing cell wall. For this system, growth seems to act as an elastic engine that drives the motions of these fibers



in a chiral manner. To be able to measure the elastic properties of cell-sized objects and to characterize the properties of this elastic engine, an optical trapping system is used to study the relaxation of a single fiber of *B. subtilis* which was bent and then released. By analyzing the relaxation time, the bending modulus of the bacterial cell wall was measured to be  $1.6 \pm 0.6 \times 10^{-12}$  erg·cm. This chapter is a modified version of a paper that was previously published as [3]. The experiments on bacterial self-propulsion were done by Neil H. Mendelson and Joelle E. Sarlls, and the physical analysis of these motions were done by Raymond E. Goldstein and myself. The laser tweezer experiments were done in collaboration with Joelle E. Sarlls and Raymond E. Goldstein.

## Chapter 2

# Twirling and Whirling: Viscous Dynamics of Rotating Filaments<sup>1</sup>

Motivated by diverse phenomena in cellular biophysics, including bacterial flagellar motion and DNA transcription and replication, this chapter studies the overdamped nonlinear dynamics of a rotationally forced filament with twist and bend elasticity. Competition between twist injection, twist diffusion, and writhing instabilities is described by a novel pair of coupled PDEs for twist and bend evolution. Analytical and numerical methods elucidate the twist/bend coupling and reveal two dynamical regimes separated by a Hopf bifurcation: (i) diffusion-dominated axial rotation, or *twirling*, and (ii) steady-state crankshafting motion, or *whirling*. The consequences of these phenomena for self-propulsion are investigated, and experimental tests proposed.

### 2.1 Statement of the Problem

Dynamics and stability of rotationally forced elastic filaments arise in several important biological settings involving bend and twist elasticity at low Reynolds number. In the context of DNA replication, when two daughter strands are produced from a duplex, it was noted [28] long ago that energy dissipation for rotations about the filament axis is so much smaller than that for transverse motions that axial “speedometer-cable” motions are favored, and are energetically and topologically feasible. During DNA transcription, in which a polymerase protein moves down the double-stranded filament, progressive unwinding of the helix can lead to an accumulation of local twist that may induce “writhing” instabilities of the filament [5, 6]. Energetic and dynamical aspects of these processes are of great current interest [7, 29].

At the cellular level, bacteria are propelled through fluids by helical flagella turned by rotary motors in the cell wall [10]. Recent studies [30, 31] have revealed the details

---

<sup>1</sup>A modified version of the work that was previously published as [1].

of two competing crystal structures assumed by flagellin, the protein building block of flagella, corresponding to helices of opposite chirality. Both local and distributed torques can change the conformation of flagella; during swimming these motors episodically reverse direction [32], and the resultant torques can induce transformations between these states [8], while uniform flow past a pinned flagellum may induce such chirality inversions [11].

To elucidate fundamental processes common to these systems, we consider here the model problem shown in Fig. 2.1: a slender elastic filament in a fluid of viscosity  $\eta$ , rotated at one end at frequency  $\omega_0$  with the other free. We study competition between three processes: twist injection at the rotated end, twist diffusion, and writhing. Analytical and numerical methods reveal two dynamical regimes of motion: *twirling*, in which the straight but twisted rod rotates about its centerline, and *whirling*, in which the centerline of the rod writhes and crankshafts around the rotation axis in a steady state.

This work is a natural outgrowth of recent studies of forced elastica in the plane [12, 33, 34], and dynamic twist-bend coupling [35, 36, 37, 38]. The balance considered between elastic and viscous stresses complements that between elasticity and inertia in the inviscid limit (as in whirling shafts [39, 40]), where twist waves propagate [39, 41, 42, 43].

An elastic filament is characterized by its radius  $a$ , contour length  $L$ , bending modulus  $A$ , and twist modulus  $C$ . The total elastic energy cost  $\mathcal{E}$  for curvature  $\kappa$  and twist density  $\Omega$  is an integral over arclength  $s$  parameterizing the position  $\mathbf{r}(s, t)$  of the filament centerline [39],

$$\mathcal{E} = \int_0^L ds \left( \frac{A}{2} \kappa^2 + \frac{C}{2} \Omega^2 - \Lambda \right), \quad (2.1)$$

where the Lagrange multiplier  $\Lambda$  enforces local inextensibility,  $(\mathbf{r}_t)_s \cdot \mathbf{r}_s = 0$ . Thus arise two dimensionless ratios:  $\Gamma \equiv C/A$ , and the aspect ratio  $a/L$ . At zero Reynolds number, elastic forces per length  $\mathbf{f} \equiv -\delta\mathcal{E}/\delta\mathbf{r}^2$  balance the viscous drag from slender-body hydrodynamics [14]:

$$\zeta_{\parallel} \hat{\mathbf{t}} \hat{\mathbf{t}} \cdot \mathbf{r}_t + \zeta_{\perp} (\mathbf{I} - \hat{\mathbf{t}} \hat{\mathbf{t}}) \cdot \mathbf{r}_t = \mathbf{f}, \quad (2.2)$$

where  $\hat{\mathbf{t}} = \mathbf{r}_s$  is the unit tangent, and the transverse and longitudinal drag coefficients are  $\zeta_{\perp} \simeq 2\zeta_{\parallel} \simeq 4\pi\eta/[\ln(L/2a) + c]$ , with  $c$  a constant of order unity [14]. Likewise, the axial elastic torque per unit length  $m = C\Omega_s$  [38, 39] balances the local rotational drag:

---

<sup>2</sup>See Appendix B

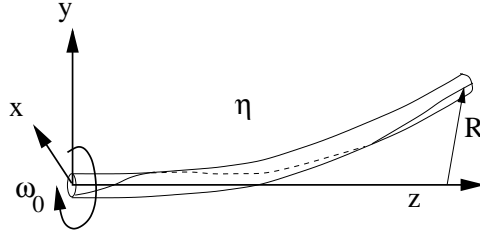


Figure 2.1: An elastic filament, rotated about  $z$  at the left end, surrounded by a fluid of viscosity  $\eta$ .

$m = \zeta_r \omega$ , where  $\omega(s, t)$  is the local rotational velocity about  $\hat{\mathbf{t}}$  and  $\zeta_r \simeq 4\pi\eta a^2$  [14]. We also define  $\epsilon^2 \equiv \zeta_r / (\zeta_\perp L^2)$ , so  $\epsilon \sim (a/L)$ , apart from logarithmic corrections.

The dynamics are closed by a geometric constraint,

$$\Omega_t = \omega_s + (-\Omega \mathbf{r}_s + \mathbf{r}_s \times \mathbf{r}_{ss}) \cdot [\mathbf{r}_t]_s, \quad (2.3)$$

which shows how twist changes due to differential rates of angular rotation, stretching (*e.g.*, extension of a straight, twisted rod decreases  $\Omega$ ), and out-of-plane bending motions (writhing) [35, 37, 36, 38]. The constraint (2.3) is a conservation law for twist density  $\Omega$ , with twist current  $-\omega$ , and with the stretching and writhing terms acting as sinks or sources. The velocities  $\omega$  and  $\mathbf{r}_t$  enter (2.3) through their space derivatives, since rigid motions cannot change  $\Omega$ . With the local torque balance  $\zeta_r \omega = C \Omega_s$  and assuming inextensibility we obtain

$$\Omega_t = \frac{C}{\zeta_r} \Omega_{ss} + \frac{1}{\zeta_\perp} \mathbf{r}_s \times \mathbf{r}_{ss} \cdot \mathbf{f}_s. \quad (2.4)$$

The second term of (2.4) is nonzero<sup>3</sup> when the filament is both out of elastic equilibrium ( $\mathbf{f} \neq 0$ ) and either nonplanar (with torsion  $\tau \neq 0$ ) or twisted ( $\Omega \neq 0$ ), and then acts as a sink or source of twist.

For boundary conditions, we assume the forced end ( $\mathbf{r}(0) = 0$ ) of the rod is clamped ( $\mathbf{r}_s(0) = \hat{\mathbf{z}}$ ) and the free end experiences no force or torque ( $\mathbf{r}_{ss}(L) = \mathbf{r}_{sss}(L) = 0; \Omega(L) = 0$ ). Local torque balance sets  $\Omega_s(0) = \zeta_r \omega_0 / C$ .

## 2.2 Dimensional Analysis

Before solving these PDE's numerically, we use dimensional analysis to understand the main features of the motion. We focus on small-amplitude bend and twist deformations

<sup>3</sup>See Appendix B

of a straight filament (thus ignoring  $\zeta_{||}$ ). Of the seven parameters  $(A, C, L, a, \zeta_r, \zeta_{\perp}, \omega_0)$ , four remain after introducing  $\Gamma$  and  $\epsilon$  and noting that  $a$  only appears through  $\zeta_r$ , so suitable rescalings of length, time, and  $\Omega$  leave only one control parameter. This can be chosen proportional to the rotation frequency  $\omega_0$ .

For low turning rates  $\omega_0$ , the filament remains straight, with twist diffusion and injection balancing. The twist density at the clamped end follows from a balance of viscous and elastic twisting torques,  $\zeta_r \omega_0 L \sim C\Omega$ , or

$$\Omega(0) \sim \frac{\zeta_r \omega_0 L}{C} \equiv \Omega_0 . \quad (2.5)$$

Instability occurs when the twist torque  $C\Omega$  is comparable to the filament buckling torque  $A/L$  [39]. At this point, the balance of viscous and twist torques (2.5) implies

$$\omega_c \sim \frac{A}{\zeta_r L^2} \sim \left(\frac{a}{L}\right)^2 \frac{E}{\eta} \sim \frac{k_B T}{\zeta_r L_p} \left(\frac{L_p}{L}\right)^2 , \quad (2.6)$$

where the second and third result follow from the relations  $A = (\pi/4)a^4 E$  between the bending modulus and the Young's modulus  $E$  [39] and  $A = k_B T L_p$ , with  $L_p$  the persistence length. Interestingly,  $\omega_c$  is independent of the twist modulus  $C$ , and since the twist density scales with the drag,  $\omega_c$  varies inversely with  $\zeta_r$ .

The result (2.6) is central, for naive dimensional analysis predicts  $\omega_c \sim E/\eta$ . With  $E \sim 10^7$  dynes/cm<sup>2</sup> and  $\eta \sim 0.01$  Poise as for rubber in water,  $\omega_c$  would be enormous if not for the prefactor  $(a/L)^2$ . Since  $a/L$  is reasonably  $10^{-3}$ , we find  $\omega_c \sim 10^3$  s<sup>-1</sup>, similar to flagella rotation rates [10] and achievable in the laboratory. The rightmost form in (2.6) shows readily the frequency scales for systems of varying length and stiffness. Consider the elastica DNA ( $L_p \sim 5 \times 10^{-6}$  cm,  $a \sim 10^{-7}$  cm), microtubules ( $L_p \sim 0.5$  cm,  $a \sim 10^{-6}$  cm), and bacterial filaments ( $L_p \sim 25$  cm,  $a \sim 3 \times 10^{-5}$  cm) [44]. The frequencies  $k_B T / \zeta_r L_p$  are then  $8 \times 10^6$  s<sup>-1</sup>,  $0.8$  s<sup>-1</sup>, and  $1.3 \times 10^{-5}$  s<sup>-1</sup>, respectively. Thus, for the instability to appear at, say,  $10^3$  s<sup>-1</sup> requires a minimum ratio  $L/L_p$  of 90, 0.03, and  $10^{-4}$ . A strand of DNA with  $L/L_p \sim 10^2$  is clearly not straight in isolation, so this instability would be hard to realize in DNA, but the stiffer examples of microtubules and bacterial filaments are indeed candidates.

Linearizing (2.2) and (2.4) about a straight filament along  $\hat{\mathbf{z}}$ , with  $\mathbf{r} \approx \hat{\mathbf{z}}s + \mathbf{r}_{\perp}$ , we see that twist diffuses with diffusion constant  $C/\zeta_r$ , while the backbone obeys a ‘‘hyperdiffusion’’ equation  $\zeta_{\perp} \mathbf{r}_{\perp t} = -A \mathbf{r}_{\perp s s s s} + C \hat{\mathbf{z}} \times (\Omega \mathbf{r}_{\perp s s})_s$ . For crankshafting motions, we

Material	$L_p$ (cm)	$k_B T / \zeta_r L_p$ ( $s^{-1}$ )	$(L/L_p)$
DNA	$5 \times 10^{-6}$	$8 \times 10^6$	90
microtubules	0.5	0.8	0.03
bacterial filaments	25	$1.3 \times 10^{-5}$	$10^{-4}$

Table 2.1: Critical Twirling Lengths for Different Biological Filaments Assuming a Twirl-to-Whirl Frequency of  $10^3 \text{ s}^{-1}$ .

set  $\mathbf{r}_{\perp t} = \chi \hat{\mathbf{z}} \times \mathbf{r}_{\perp}$ . Thus we find two characteristic lengths [12],

$$\ell_{\perp}(\chi) = (A/\zeta_{\perp}\chi)^{1/4} \quad \text{and} \quad \ell_r(\omega_0) = (C/\zeta_r\omega_0)^{1/2} . \quad (2.7)$$

These are analogous to the penetration depth in the familiar theory of oscillations in a viscous fluid [13]. The primary instability is given by  $\ell_r(\omega) \sim L$ .

The crankshafting frequency  $\chi$  for whirling can be estimated by assuming that the transverse drag,  $\zeta_{\perp}\chi|\mathbf{r}_{\perp}|$ , is roughly equal to the elastic force per length,  $A|\mathbf{r}_{\perp 4s}| \sim A|\mathbf{r}_{\perp}|/L^4$ . Thus  $\chi \sim A/\zeta_{\perp}L^4 \sim (a/L)^2\omega_c$  ( $C \approx A$  for typical materials [39]), and  $\ell_{\perp}(\chi) \sim \ell_r(\omega_c) \sim L$  at the transition. The whirling rod does not undergo simple rigid body rotation; the speedometer-cable rotational motion is faster than the backbone crankshafting motion by a factor of  $(L/a)^2$ . This steady-state shape is possible because diffusion can homogenize the twist as fast as backbone motion relieves it. We describe this process quantitatively by integrating (2.3) along the rod for inextensible, steady-state ( $\Omega_t = 0$ ) crankshafting. The difference  $\Delta\omega$  in rotational velocities about the local tangents at  $s = L$  and  $s = 0$  is

$$-\Delta\omega = \chi[1 - \hat{\mathbf{z}} \cdot \hat{\mathbf{t}}(L)]. \quad (2.8)$$

Equivalently,  $\Delta\omega$  is the injected twist current minus the twist current leaving the free end. Thus, writhing acts as a twist sink in steady-state crankshafting motion when the rod's free end is not aligned with the  $z$ -axis.

When the twist diffusion time,  $\zeta_r \ell_{\perp}^2(\chi)/C$ , is longer than the bending time  $\chi^{-1}$ , buckling can relieve twist faster than it is replenished by diffusion, and steady-state crankshafting would likely be unstable. One possible new behavior would consist of repeated sequences of transient whirling followed by quiescence as twist builds up anew. The scaling argument above yields  $\chi \sim E/\eta$ , a factor of  $\epsilon^{-4}$  higher than the rate at onset of the first instability, and thus unreachable for typical materials.

The bend relaxation time suggests the rescaling,

$$\tilde{t} \equiv (A/\zeta_{\perp}L^4) . \quad (2.9)$$

A natural pair of further rescalings of (2.4) is  $\tilde{s} = s/L$ , and  $\tilde{\Omega} = \Omega L$ . If we parameterize the filament centerline (Fig. 2.1) as  $\mathbf{r}(s, t) = (X(s, t), Y(s, t), s - \delta(s, t))$ , introduce the complex transverse displacement  $\xi = (X + iY)/L$ , and expand the dynamics up to third order in  $\xi$  (immediately dropping the tildes), we obtain

$$\begin{aligned} \xi_t &= -\xi_{4s} - (\Lambda\xi_s)_s + i\Gamma [\Omega (\xi_{ss}(1 - \delta_s) + \delta_{ss}\xi_s)]_s \\ &\quad - \left[ \frac{1}{2} (\xi_{4s}^*\xi_s + \xi_{4s}\xi_s^*) + \Lambda_s \right] \xi_s \\ \Omega_t &= \frac{\Gamma}{\epsilon^2} \Omega_{ss} + \frac{1}{2} [i (\xi_{5s}^*\xi_{ss} - \xi_{5s}\xi_{ss}^*) \\ &\quad + \Gamma ((\Omega\xi_{ss}^*)_{ss} \xi_{ss} + (\Omega\xi_{ss})_{ss} \xi_{ss}^*)] , \end{aligned} \quad (2.10)$$

where the inextensibility constraint  $(1 - \zeta_{\parallel}/\zeta_{\perp})(\mathbf{r}_{ss} \cdot \mathbf{f}) + (\mathbf{r}_s \cdot \mathbf{f}_s) \simeq \frac{1}{2}(\mathbf{r}_{ss} \cdot \mathbf{f}) + (\mathbf{r}_s \cdot \mathbf{f}_s) = 0$  is expanded to set  $\Lambda$  as

$$\left( \Lambda - \frac{3}{2} |\xi_{ss}|^2 \right)_{ss} = \frac{1}{2} (\mathcal{R}e(\xi_{4s}\xi_{ss}^*) + i\Gamma\Omega\mathcal{I}m(\xi_{3s}\xi_{ss}^*)).$$

This constraint also fixes  $\delta_s \simeq \frac{1}{2}|\xi_s|^2$ . As anticipated, apart from material properties  $\Gamma$  and  $\epsilon$ , the coupled twist/bend dynamics are governed by a single control parameter  $\omega_0$ , which appears only in the (rescaled) boundary condition,  $\Omega_s(0) = \epsilon^2\omega_0/\Gamma = \alpha$ . The PDEs (2.10) are like those of excitable media [45], with a separation of time scales derived from the aspect ratio  $\epsilon$ . For the usual case  $\epsilon \ll 1$ , twist is the fast variable and bends are slow.

### 2.3 Linearized Dynamics

The twist profile in the straight filament ( $\xi = 0$ ) satisfies  $\Omega_t = \Omega_{ss}$ . After transients die out, the steady-state profile is linear in  $s$  [7],  $\Omega = (\zeta_r\omega_0/C)(s - L)$ . Using this in the linearized filament evolution and taking  $\xi(s, t) = \xi(s) \exp(i\chi t)$ , a rigidly rotating, neutrally stable shape, we obtain<sup>4</sup>

$$\chi\xi = i\xi_{4s} + \Gamma\alpha[(s - 1)\xi_{ss}]_s . \quad (2.11)$$

---

<sup>4</sup>See Appendix C

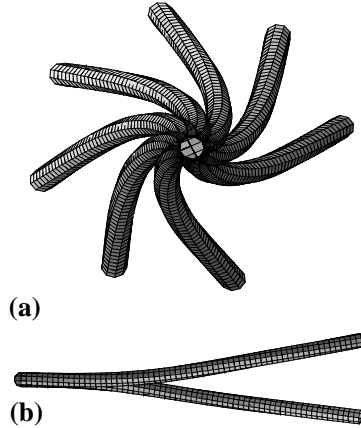


Figure 2.2: (a) Stroboscopic montage of the “whirling” filament, viewed from along the  $z$ -axis, as it rotates clockwise; (b) side view at two times.

Numerical solution [46] of (2.11) yields a critical value  $\alpha_c \simeq 8.9/\Gamma$  (confirming dimensional analysis of Eq. (2.9)), below which the rod is straight and executes only axial rotation (“twirling”), and above which the rod buckles and rotates (“whirls”) at a frequency which for  $\alpha \simeq \alpha_c$  is  $\chi \approx 2.32\Gamma\alpha$ . This motion is the dynamical equivalent of the static writhing instability of a twisted elastica [39]. Inserting all numerical factors, the critical frequency and rotation rate (at onset) are

$$\omega_c \simeq 0.563 \left(\frac{a}{L}\right)^2 \frac{E}{\eta}, \quad \chi_c \simeq 20.9 \left(\frac{a}{L}\right)^2 \omega_c. \quad (2.12)$$

These solutions for  $\omega_c$  and  $\chi$  are for the first linearly stable mode. There also exist other modes that become linearly excited at higher values of the turning frequency. Interestingly, when these modes were found numerically, it was seen that the growth rates and turning frequencies for the different modes interact. It was observed that all the modes’ growth rates initially increase quadratically in the turning frequency. This can be shown analytically by treating the twist coupling as a perturbation<sup>5</sup>. The first mode growth rate begins negative and increases. At the critical value of the turning frequency, it passes through zero and continues climbing. The second mode growth rate begins more negative, but grows faster. At a value of the turning frequency of about  $1.5\omega_c$ , the second mode growth rate surpasses the first mode, however, shortly before this point, the first mode

<sup>5</sup>See Appendix C



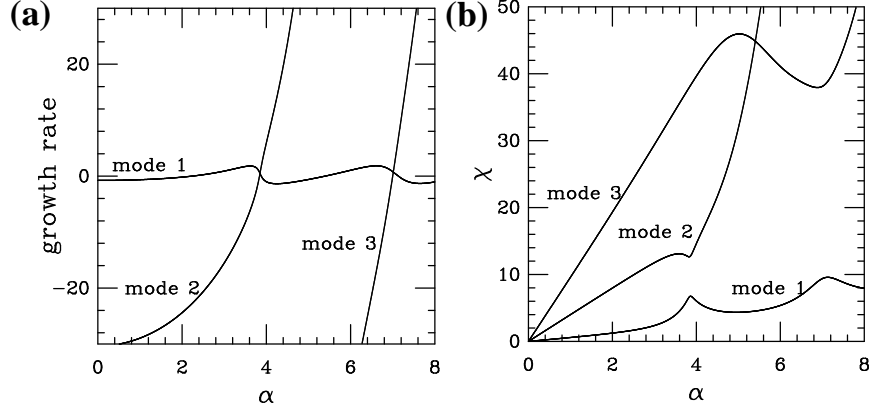


Figure 2.3: (a) Growth rates for the first three modes of the linear equation. Mode becomes unstable when the growth rate is positive. (b) Whirling frequencies for the first three modes.

---

dips down and goes negative again. This dipping behavior is observed every time a new mode becomes linearly stable, creating an oscillating behavior in the first mode growth rate. It is also seen that the  $\chi$  values for different modes seem to attract one another. At the point when the growth rate of one mode approaches that of another, the lower mode  $\chi$  will increase sharply and the higher mode will decrease. After the two modes growth rates have passed one another, the lower mode  $\chi$  decreases rapidly and the higher one increases anew. It is believed that this behavior is related to energy level attraction and repulsion in quantum mechanical systems such as is seen in molecular energy spectra. This view has not yet been exploited, though.

## 2.4 Weakly Nonlinear Theory

Numerical solution of (2.10) with a pseudospectral method [38, 47] shows that there is indeed a steady state beyond the bifurcation. As  $\alpha - \alpha_c$  increases, the shape becomes more helical. The free end of the whirling filament experiences more drag than points closer to the driven end and thus lags behind (Fig. 2.2). Since  $\Omega$  depends quadratically on the backbone shape (see Eq. 2.3), near  $\omega_c$ , where  $\xi$  is small, the twist density remains nearly linear in  $s$ . Numerical studies show that the free end traces out a circle with

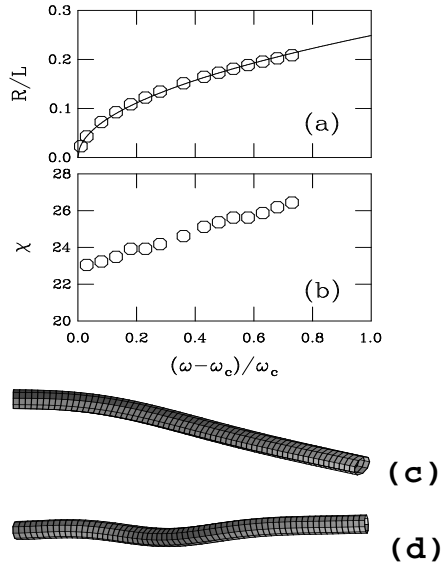


Figure 2.4: (a) Amplitude  $R$  (with a square root fit) and (b) cranksafting frequency of filament tip motion as a function of frequency offset from primary instability. (c) and (d); filament shapes for  $(\omega - \omega_c)/\omega_c = 0.27$  and  $3.52$ , with  $\Gamma = 1$ .

radius  $R \sim (\omega - \omega_c)^{1/2}$ : a supercritical Hopf bifurcation [45]. This can be understood from (2.8) and dimensional arguments for the displacement;  $[1 - \hat{\mathbf{z}} \cdot \hat{\mathbf{t}}(L)] \simeq (R/L)^2$ , so  $\omega(0) - \omega(L) \sim \chi(R/L)^2$ . The twist that can be relieved by diffusion is limited, so  $\omega(L) \approx \omega_c$ . From the linear dynamics,  $\chi \sim \omega_c$ , leading to  $R \sim (\omega_0 - \omega_c)^{1/2}$ .

## 2.5 Swimming

Chirality of the whirling filament breaks time-reversal invariance of the motion, thereby allowing [48, 49] a net propulsive force  $F_p$  along  $\hat{\mathbf{z}}$  to be generated. The elastic propulsive force density is a total derivative, so the total force is expressible in terms of the filament properties at its ends. For the clamped/free boundary conditions used here,  $F_p = -\mathbf{r}_{3s}(0) \cdot \hat{\mathbf{z}} - \Lambda(0) = \mathbf{r}_{ss}(0) \cdot \mathbf{r}_{ss}(0) - \Lambda(0)$ . As shown in Fig. 2.5,  $F_p$  rises linearly from zero near the bifurcation, as it is quadratic in the transverse displacement, which in turn has the supercritical form shown in Fig. 2.4(a). While we know of no organism that utilizes this precise mechanism for self-propulsion, there is evidence for self-propulsion associated with twist-induced whirling in growing bacterial macrofibers constrained at one end in certain

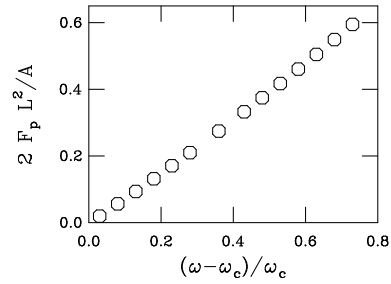


Figure 2.5: Propulsive force generated by steady-state whirling motions, as a function of driving frequency.

---

laboratory experiments [3]. Experiments are underway to explore further this possible connection.

The possibility of observing instabilities driven by twist accumulation along an elastica hinges upon a balance of material properties, fluid viscosity, and adequate forcing. Flow- and rotation-induced bacterial flagellar conformational transitions [32, 8, 11] provide proof-of-principle that this balance can be achieved *in vivo*. Like flagella, fibers of *B. subtilis* cells have adequate material properties (e.g. Young's modulus [44]) and aspect ratio to display instabilities like those described here. More complex phenomena are associated with instabilities of helical flagella, as described elsewhere [50].

## Chapter 3

### Bistable Helices<sup>1</sup>

This chapter extends elasticity theory of filaments to encompass systems, such as bacterial flagella, that display competition between two helical structures of opposite chirality. A general, fully intrinsic formulation of the dynamics of bend and twist degrees of freedom is developed using the natural frame of space curves, spanning from the inviscid limit to the viscously-overdamped regime applicable to cellular biology. Aspects of front propagation found in flagella are discussed.

#### 3.1 Bacterial Flagellar Flipping

Over three and a half billion seconds ago, Kirchhoff presented the fundamental equations for elastic rods, the basis for most subsequent theory on the statics and dynamics of elastic filaments [4]. For at least as many *years*, terrestrial life forms have been engineering and generating all manner of elastic rods, one of the key structural elements of single and multicellular life. It is likely, therefore, that biology has much to teach us about the rich phenomena and inherent possibilities contained within the basic framework of elasticity theory. Here we report one such lesson, namely, the peculiar case of flip-flops of chirality in helical, elastic filaments. The most well-known example of these transitions occurs when the motors that turn helical bacterial flagella reverse direction, causing a coherent bundle of nestled flagella to unbundle and the cell body to tumble [8]. Likewise, when such flagella are placed in an external fluid flow, it is observed that regions within the filament periodically flip to the opposite chirality, and that those flipped domains propagate steadily downstream [11]. In quiescent fluids, flagella may display two coexisting chiralities (see Fig. 3.1a). Bacterial fibers [15], chains of bacterial cells formed by repeated cell division without separation, may also display coexistence of two helix hands (Fig. 3.1b) [18]. Another example, an order of magnitude smaller, involves two distinct

---

<sup>1</sup>A modified version of the work that was previously published as [2]

conformations of DNA. Recent experiments [51, 52] indicate stretches of left-handed Z-DNA forming spontaneously from right-handed B-DNA due to the stresses generated by twisting during the process of transcription [53, 54, 55, 29].

We present here a simple theory of helical bistability [50, 56], treating it as competition between two states, each locally stable, but of opposite handedness [57]. This differs fundamentally from the phenomenon of *perversion*, seen in vines [58], in which external constraints produce chirality. The bistability of molecular units in bacterial flagella, first advanced by Asakura [24] and later concretely realized as a model by Calladine [22, 23], can be viewed as underlying the continuum approach presented below. Assuming such an underpinning, we extend the energetic formulation of linear elasticity theory by introducing a Landau-Ginzburg functional in the twist strains [59, 60] and, building on earlier work [62, 61, 35, 36, 37, 38, 63] develop a fully *intrinsic* formulation of the kinematics and dynamics applicable to arbitrary twist-energy functionals. Finally, we describe elementary front solutions linking bistable helical states and discuss their biological significance.

The material frame of a filament is an orthonormal triad  $\{\hat{\mathbf{e}}_1, \hat{\mathbf{e}}_2, \hat{\mathbf{e}}_3\}$ , where we choose  $\hat{\mathbf{e}}_3$  along the tangent,  $\hat{\mathbf{e}}_1$  pointing toward an imaginary line on the rod surface, and  $\hat{\mathbf{e}}_2 = \hat{\mathbf{e}}_3 \times \hat{\mathbf{e}}_1$ . The strain vector  $\mathbf{\Omega}(s) = (\Omega_1, \Omega_2, \Omega_3)$  characterizes the shape of the filament through the kinematic relation  $\partial_s \hat{\mathbf{e}}_i = \mathbf{\Omega} \times \hat{\mathbf{e}}_i$ , and the curvature  $\kappa$  satisfies  $\kappa^2 = \Omega_1^2 + \Omega_2^2$ , with  $\Omega_3$  the twist density. We expect the elastic energy  $\mathcal{E}[\mathbf{\Omega}]$  to be a Landau expansion,  $\mathcal{E} = \sum A_{ij} \Omega_i \Omega_j + \sum B_{ijk} \Omega_i \Omega_j \Omega_k + \dots$ , where symmetry considerations dictate the allowed elastic constants  $A_{ij}$ , etc. [59, 60, 64]. In *linear* elasticity theory for an isotropic cylindrical rod, the *straight, untwisted* rod minimizes the elastic energy  $\mathcal{E} = (1/2) \int ds (A\kappa^2 + C\Omega^2)$ , where we adopt the shorthand  $\Omega \equiv \Omega_3$ . A *helix* is the ground state if the minima of both the curvature and twist energy costs are shifted from zero to *intrinsic curvatures*  $\Omega_1^0, \Omega_2^0$ , and *intrinsic twist*  $\Omega^0$ . Perhaps the simplest model for a *bistable helix* has an energy with a preferred curvature and *two* stable twist states,

$$\mathcal{E} = \int ds \left[ \frac{A}{2} \left( (\Delta\Omega_1)^2 + (\Delta\Omega_2)^2 \right) + \frac{\gamma^2}{2} \Omega_s^2 + V(\Omega) \right], \quad (3.1)$$

where  $\Delta\Omega_i = \Omega_i - \Omega_i^0$ ,  $V(\Omega)$  is a double-well potential and the twist-gradient coefficient  $\gamma$  controls the width of fronts connecting the two states. A most intriguing feature of such fronts is that they correspond to helices concatenated at an angle, as in the examples of Fig. 3.1.

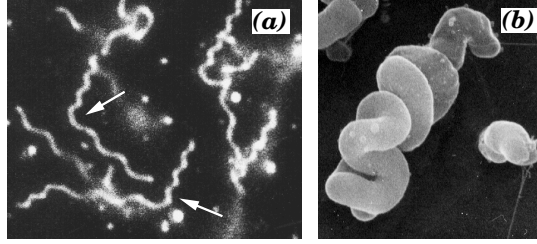


Figure 3.1: Bistable helices. (a) Flagella of *Salmonella*, with coexisting left- and right-handed helices (arrows), courtes of H. Hotani. (b) Solenoidal form of *B. subtilis* fiber, with coexisting helices, courtesy of M. Tilby.

How do we link such an energy functional to the filament dynamics? The arclength kinematics of the material frame have a complementary temporal kinematics,

$$\partial_t \hat{\mathbf{e}}_i = \boldsymbol{\omega} \times \hat{\mathbf{e}}_i \quad (3.2)$$

with  $\boldsymbol{\omega}$  the rotation rate. It is convenient to trade the material for a “natural” frame  $\epsilon$  [38], and use related complex strain and rotation rates,

$$\epsilon = (\hat{\mathbf{e}}_1 + i\hat{\mathbf{e}}_2)e^{i\vartheta} \quad (3.3)$$

$$\Psi \equiv \hat{\mathbf{e}}_{3,s} \cdot \epsilon = (-i\Omega_1 + \Omega_2)e^{i\vartheta} \quad (3.4)$$

$$\Pi \equiv \hat{\mathbf{e}}_{3,t} \cdot \epsilon = (-i\omega_1 + \omega_2)e^{i\vartheta} \quad (3.5)$$

where  $\vartheta(s, t) = \int^s ds' \Omega$ . As they describe the filament shape and velocity,  $\Psi$  and  $\Pi$  are related to position and momentum variables in a “Hamiltonian” dynamics (below). (Note that a helix of curvature  $\kappa$  and torsion  $\tau$ , having then radius  $R = \kappa/(\kappa^2 + \tau^2)$  and pitch  $p = 2\pi\tau/(\kappa^2 + \tau^2)$ , corresponds to  $\Psi = \kappa \exp(i\tau s)$ .) The kinematics of the natural frame can now be written as:

$$\begin{aligned} \partial_s \hat{\mathbf{e}}_3 &= \Re(\Psi \epsilon^*) , & \partial_s \epsilon &= -\Psi \hat{\mathbf{e}}_3 \\ \partial_t \hat{\mathbf{e}}_3 &= \Re(\Pi \epsilon^*) , & \partial_t \epsilon &= -\Pi \hat{\mathbf{e}}_3 + i(\vartheta_t - \omega)\epsilon , \end{aligned} \quad (3.6)$$

where we again simplify the notation:  $\omega \equiv \omega_3$ . The quantities that describe completely the configuration of an elastic filament are now  $\Psi$  and  $\Omega$ , representing the backbone shape and the twist. Using the commutator,  $\partial_t \partial_s = \partial_s \partial_t - [\hat{\mathbf{e}}_3 \cdot \mathbf{r}_{t,s}] \partial_s$ , with  $\mathbf{r}$  the vector that describes the filament centerline, the kinematic equations become<sup>2</sup>

$$\Omega_t = \omega_s - \Omega \hat{\mathbf{e}}_3 \cdot \mathbf{r}_{t,s} + \Im(\Psi^* \Pi) \quad (3.7)$$

<sup>2</sup>See Appendix G

$$\Psi_t = \Pi_s - \Psi \hat{\mathbf{e}}_3 \cdot \mathbf{r}_{t,s} + i\Psi \int^{s'} ds' \Im(\Psi^* \Pi) . \quad (3.8)$$

The successive terms in (3.7) and (3.8) describe how differential rotation rates cause strain accumulation, the coupling with stretching, and a coupling between twisting and writhing motions. Since  $\Im(\Psi^* \Pi) = (\mathbf{r}_s \times \mathbf{r}_{ss}) \cdot \mathbf{r}_{t,s}$ , the  $\Omega$  equation is equivalent to that found in [1, 35]. These purely geometrical relations apply to any moving filament, regardless of the forces that are present.

We close the equations by calculating the force and moment per length acting on the filament. From the principle of virtual work these are functional derivatives of the energy (3.1); the force per length is  $\mathbf{f} = -\delta\mathcal{E}/\delta\mathbf{r}$  with variations in the rotation about the tangent vector,  $\delta\chi \equiv \hat{\mathbf{e}}_2 \cdot \delta\hat{\mathbf{e}}_1$ , set to zero, while the moment per length about the tangent is  $m = -\delta\mathcal{E}/\delta\chi$  with  $\delta\mathbf{r} = 0$ . They are

$$\begin{aligned} m &= \partial_s \left( \frac{\delta\mathcal{E}}{\delta\Omega} \right) + A \Im(\Psi^* \Psi^0) \\ \mathbf{f} &= (\Re(\Phi) - \Lambda_s) \hat{\mathbf{e}}_3 + \Re(\epsilon^* \mathcal{F}_\perp) , \end{aligned} \quad (3.9)$$

with

$$\begin{aligned} \mathcal{F}_\perp &= -A \left[ \partial_{ss} (\Psi - \Psi_o) + \frac{1}{2} (|\Psi|^2 - |\Psi^0|^2) \Psi \right] \\ &\quad + i \partial_s \left( \frac{\delta\mathcal{E}}{\delta\Omega} \Psi \right) - \Lambda \Psi , \end{aligned} \quad (3.10)$$

where

$$\Psi^0 = (-i\Omega_1^0 + \Omega_2^0) e^{i\vartheta} , \quad \Phi = -A(\Psi - \Psi^0) \partial_s \Psi^{0*} , \quad (3.11)$$

and a factor of  $\frac{1}{2}\Omega^2$  has been absorbed into the Lagrange multiplier  $\Lambda$ . The second term in the moment equation describes how deformations that are out of the plane of the preferred curvature cause rotation about the tangent.

A dynamical statement is required to close the system. In a normal Newtonian description, forces and moments balance accelerations,  $\rho \mathbf{r}_{tt} = \mathbf{f}$  and  $m = I\omega_t$  with  $\rho$  a mass per length, and  $I$  a cross-sectional moment of inertia. The dynamical equations (3.9) are then the Kirchhoff equations for thin rods with nonlinear constitutive relationships [41, 66, 65]. In the presence of a transverse drag coefficient  $\zeta$ , an additional force  $\zeta \mathbf{r}_t$  appears, while the rotational drag coefficient introduces  $m = I\omega_t + \zeta_r \omega$ . This moment equation closes the twist dynamics; the backbone dynamics are found by taking a spatial

derivative and dotting the force equation with  $\epsilon$ ,

$$\rho \left[ \partial_t - 2 \int^s ds' \mathfrak{S}(\Psi^* \Pi) + 2 \hat{\mathbf{e}}_3 \cdot \mathbf{r}_{t,s} \right] \Pi + \zeta \Pi = \mathbf{f}_s \cdot \epsilon ,$$

the equivalent of the momentum equation in a Hamiltonian system. The low Reynolds number regime is attained when the mass density and moment of inertia are zero, forces and moments are balanced by velocities and angular velocities,  $\zeta \mathbf{r}_t = \mathbf{f}$  and  $m = \zeta_r \omega$ , so  $\zeta \Pi = \mathbf{f}_s \cdot \epsilon$ . Substituting these back into the  $\Omega$  and  $\Psi$  equations, and using linear elasticity theory to define the forces and moments, yields the viscous results found previously [38].

Remarkably, both stationary solutions and moving fronts between bistable states exist for all bistable potentials [50, 56]. Stationary fronts exist when the potential difference  $\Delta V$  between the twist energy minima (see Fig. 3.2) vanishes; they connect asymptotically the two stable helical states with opposite torsion and without external mechanical constraints. From (3.10) we see that the transverse force on the filament vanishes when  $\Psi = \Psi^0$  and  $\delta \mathcal{E} / \delta \Omega = 0$ , namely, when the curvatures have their intrinsic values and  $\Omega$  is one of its stable states. Then  $\Psi^* \Psi^0$  is real and the twisting moment in (3.9) vanishes. The twist profile satisfies the Euler-Lagrange equation

$$\gamma^2 \Omega_{ss} - V'(\Omega) = 0 . \quad (3.12)$$

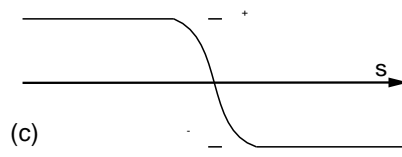
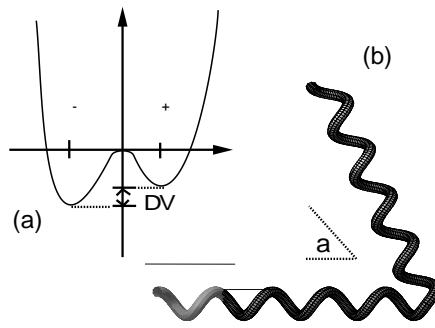
With the Landau model  $V = -(r/2)\Omega^2 + (u/4)\Omega^4$ , the solution for an infinite filament is  $\Omega(s) = \Omega^+ \tanh(s/2\xi)$ , where  $\Omega^\pm = \pm(r/u)^{1/2}$  and the front width is  $\xi = \gamma/(2r)^{1/2}$ . In the natural frame, the shape is

$$\Psi = \Omega_2^0 \exp(2i\xi\Omega^+ \log \cosh(s/2\xi)) , \quad (3.13)$$

where by suitable choice of  $\hat{\mathbf{e}}_2$  we can set  $\Omega_1^0 = 0$ . In real space, as  $s \rightarrow \pm\infty$ , this solution describes helices with curvature  $\Omega_2^0$  and torsion  $\Omega^\pm$ . To see the real-space relationship between the helices, we go to the limit  $\xi \rightarrow 0$  and solve the matching problem between one right-handed and one left-handed helix. Let the tangents to the right and left helices make angles  $\theta_\pm$  with the two (asymptotic) helical axes  $z_\pm$ . Continuity of the tangents at the junction of the two axes requires that the axes be rotated about the junction by a “block” angle  $\alpha = \pi - (\theta_+ - \theta_-)$  (Figs. 3.2 and 3.3)

$$\alpha = \tan^{-1}(\tau_+/\kappa_+) - \tan^{-1}(\tau_-/\kappa_-) , \quad (3.14)$$









their relevance for experiments, notably for flagellar systems. Our continuum approach connects the phenomenon of bistability at the scale of nanometers [22, 23, 10, 30], with the bistability observed at tens of microns [11, 26]; it points out, as well, the need for experiments on the rates of chirality transformations under defined conditions of torques and flows, and it provides the possibility for a new level of quantitative description bridging the microscopic and macroscopic observations.

## Chapter 4

### Experiments on *B. subtilis* Fibers <sup>1</sup>

Supercoiling motions that accompany the growth of bacterial macrofibers (multicellular filamentous structures formed in *B. subtilis* by cell division without separation) are responsible for rolling, pivoting, and walking of fibers on a surface. Fibers possess a fulcrum about which they pivot and step in a chiral manner; forces and torques associated with cell growth, when blocked by friction, result in self-propulsion. The elastic engine that drives macrofiber motions generates torques estimated as micro-dyne-cm and femtowatts of power; optical trapping studies yield a first direct measurement of the Young's modulus of the bacterial cell wall, the engine's "working fluid," of *ca.* 5.0 MPa.

#### 4.1 Basics

This chapter focuses on the discovery that supercoiling motions of growing multicellular bacterial structures result in chiral self-propulsion when they are in contact with a solid surface. These structures, termed *macrofibers*, arise by repetitive supercoiling of an elongating chain of linked cells (a *filament*) or filament bundle that twists as it grows [15, 72]. Individual rodlike cells,  $4\mu\text{m} \times 0.7\mu\text{m}$ , grow only in length, so the cell filaments, produced in a mutant of *B. subtilis* by failure of cell separation after each growth and division cycle, are of uniform diameter. They self-assemble into macrofibers millimeters in length and tenths of millimeters in diameter [73, 16]; the mature structure consists of a single long filament folded repeatedly upon itself and twisted into a fiber shaft that is capped at both ends with loops. Macrofiber helix hand and degree of twist are governed by genetic and environmental factors such as temperature and the concentration of certain ions in the growth fluid [20].

The results reported here show that the twisting and writhing dynamics underlying supercoiling can constitute the workings of an *elastic engine* that powers chiral self-propulsion. Unlike other self-propulsion systems that operate at low Reynolds numbers and are

---

<sup>1</sup>A modified version of the work that was previously published as [3].

based upon periodic movement of objects with fixed underlying shape or shape sequences [74], such as helical flagella turned by rotary motors or flexible flagella driven by local or distributed bending moments [48, 49, 33, 34], macrofiber motions require increase in length. Several qualitative models have been advanced to explain the origin of twisting and supercoiling associated with growth [73, 16, 75, 76, 18, 36, 77]. The assembly of peptidoglycan, the strength-bearing cell wall polymer, is believed essential [75, 78, 76, 79]; but no definitive link between microscopic properties, such as the geometry of glycan orientation in the wall or its viscoelasticity, and the filament twisting with cell elongation has yet been established. A molecular model thus cannot yet be offered for the workings of this macrofiber elastic engine. By characterizing its output we hope to learn more about the ways in which it powers fiber self-assembly and other kinds of work, and also shed light on the polymer physics of bacterial cell walls and its link to cell growth.

Supercoiling of bacterial filaments may occur with *open* strands, thus in the absence of the topological constraint of fixed linking number that plays so crucial a role in the conformation [80, 81, 82] and dynamics of DNA and other twisted filaments [35, 36, 41]. Bacterial filaments are so stiff that the thermal fluctuations important in the statistical mechanics of DNA [83, 84] also play no role. With fiber lengths typically on the order of 0.05 cm and velocities of  $2 \times 10^{-3}$  cm/s, the Reynolds number is at most  $\mathcal{O}(10^{-2})$ , so these phenomena occur without inertia – purely through a balance between elastic, body, and viscous forces.

## 4.2 Chiral Self-Propulsion on a Solid Surface

The macrofibers used in these studies cannot swim or swarm, and no visible flagella structures can be found on their cell walls. They are however capable of slow movement over solid surfaces. Fibers make contact with the floor of a growth chamber because they are slightly more dense than the growth medium in which they move. To study fiber motions on a surface a dual-view microscope system was constructed that permits simultaneous visualization of fiber contact with the surface and location within the chamber (Fig. 4.1). The growth chamber was illuminated both from below and the side with two light pipes from a single fiber optic light source (Dolan-Jenner, Inc.). Videos were made using two CCD cameras (Cohu); one fitted to an Olympus SZ-Tr zoom stereo microscope above the growth chamber, the other to a Bausch & Lomb monocular compound microscope

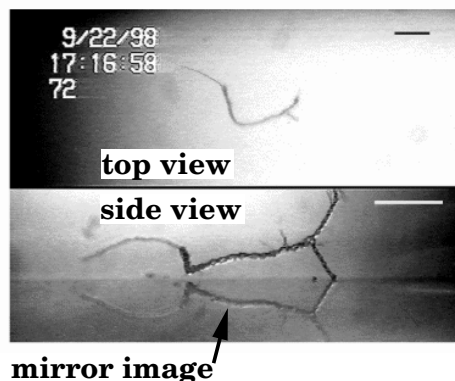


Figure 4.1: Images of macrofibers from top and side within a glass growth chamber. Scale bar is 0.5 mm.

tube aimed horizontally. The side-view images obtained from the latter always appear as mirror images due to reflection by the glass surface upon which the bacterial structures rest. Images were transferred to a Phase Eight screen splitter (Vicon Industries, Inc.) and the synchronized output sent to a GYYR time-lapse recorder (Odetics, Inc.). Motion dynamics were measured by comparison of individual frames directly using overlays on a video monitor screen, or following transfer to a PC using Image Pro Plus software (Media Cybernetics).

Motions of both right, and left-handed structures were examined [85] using *Bacillus subtilis* strains FJ7 and RHX [21]. Right-handed FJ7 fibers were produced by overnight growth in 10 ml of TB [86] containing  $5 \times 10^{-2}$ M  $\text{MgSO}_4$  at  $20^\circ$  C. A single intact fiber was transferred into medium of the same composition in the glass growth chamber and the top was covered with two glass slides. For petri dish cultures, viewed only from above, a single fiber was disrupted by toothpick transfer into medium of the same composition. Both glass chamber and petri dish cultures were grown on a microscope stage at  $24^\circ$  C. Left-handed RHX fibers were produced similarly using TB containing  $5 \times 10^{-2}$ M  $(\text{NH}_4)_2\text{SO}_4$ .

Macrofibers underwent three kinds of motions as they grew on a solid surface: rolling, pivoting, and walking. Fig. 4.2 shows that rolling is caused by twisting of a fiber about its shaft as it elongates. If the shaft and its terminal loop lie flat on the surface, twisting and friction result in propulsion. The terminal loop rises onto its edge then returns to the floor upside down at a slightly displaced position. The net result is rolling in a

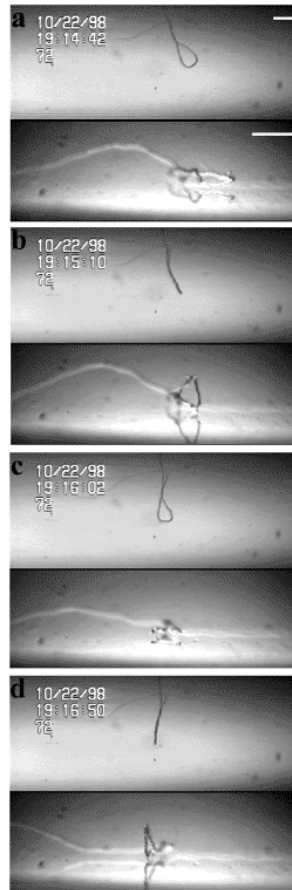


Figure 4.2: Rolling sequence. Dual-view images showing motion of a macrofiber. Panels are at times (b) 28 s., (c) 80 s., and (d) 128 seconds after (a). Scale bar is 0.5 mm.

direction determined by the handedness of helix twisting. In Fig. 4.2, the lower half of each panel (the side view) shows the terminal loop of a right-hand fiber viewed end-on as it rolled to the left through  $270^\circ$  while the loop twisted in a counterclockwise direction. The corresponding top view images (upper half of each panel) reveal that during this sequence the fiber shaft pivoted clockwise. Other, low-magnification films show that the entire fiber shaft pivots in a helix-hand-specific direction (RH fibers clockwise, LH fibers counterclockwise). Rolling and pivoting are therefore inherent properties of macrofiber hand, not products of convection currents or other external forces.

Pivoting motions reveal that fibers possess a fulcrum midway along their length that effectively divides them into two mechanical halves [85]. During growth each half rotates



in a direction opposite to the other. Figure 4.3a shows rates of CW and CCW pivoting in RH and LH structures, respectively. Figure 4.3b shows the corresponding rates of fiber length increase during pivoting. Repetitive periodic supercoiling, required for macrofiber morphogenesis, is responsible for the length reduction shown in Fig. 4.3b (the right-hand structure). After each supercoiling the newly formed structure must increase its length again before it undergoes another supercoiling and length reduction [75, 76]. A symmetry argument can be advanced to explain the direction of fiber pivoting (Fig. 4.3c). There are two fundamental vectors in the problem, the surface normal  $\mathbf{n}$  about which pivoting occurs at the fulcrum marked by a dashed line in Fig. 3c, and the helicity vector  $\mathbf{h}$  defining the twisting direction of the fiber. The pivoting vector  $\mathbf{p}$  should be composed of these; the unique choice is  $\mathbf{p} = \mathbf{n} \times \mathbf{h}$ , which lies in the plane pointing in the direction that the frictional force of the surface acts to oppose the twisting motion. The vectors  $\mathbf{p}$  so constructed for the two fiber ends are in opposite directions, leading to rotational motion. A composite of images taken from above (Fig. 4.3d) illustrates the overall pivoting motion. Both rolling and walking motions of half-fibers drive pivoting. The steps taken during walking (rectilinear motion) occur when part of a fiber rises off the surface then returns to it elsewhere [85].

To determine the magnitude of viscous forces involved in fiber motion we model it as a straight, rigid rod rotating at angular speed  $\omega$  about a pivot at one end. The force density acting on the fiber moving with local velocity  $v$  is  $\zeta_{\perp} v = \zeta_{\perp} \omega s$  where  $s$  is the distance along the fiber from the pivot,  $\zeta_{\perp} \simeq 4\pi\eta/\ln(L/a)$  is the drag coefficient for motion perpendicular to the fiber axis [87],  $\eta$  the fluid viscosity,  $L$  the fiber length and  $a$  its radius. The torque per unit length  $\zeta_{\perp} \omega s^2$  yields a total torque  $\tau_{\perp} = \zeta_{\perp} \omega L^3/3$ . Data on two separate walking motions yield  $\omega = 0.103 \text{ rad} \cdot \text{s}^{-1}$  with  $L = 0.73 \text{ mm}$ , and  $\omega = 0.029 \text{ rad} \cdot \text{s}^{-1}$  with  $L = 1.65 \text{ mm}$ . The corresponding torques are  $1.7 \times 10^{-6} \text{ erg}$  and  $5.4 \times 10^{-6} \text{ erg}$ , respectively. Both are significantly larger than gravitational torques acting on the structures studied, estimated by the same reasoning to be  $\tau_g \simeq \pi a^2 \delta \rho g L^2/2 \simeq 6 \times 10^{-7} \text{ erg}$ , where  $\delta \rho$  is the density difference between the fiber of radius  $a \simeq 0.002 \text{ cm}$  and the surrounding fluid [88].

Continuing in this manner, we estimate the power generation by these motions to be  $P = \tau_{\perp} \omega$ . With the values for  $L$ ,  $\omega$ , etc. used above we find  $P \sim 2 \times 10^{-14} \text{ Watts}$ . Scaling by the filament volume the power density is approximately  $20 \text{ nW/cm}^3$ . For comparison,

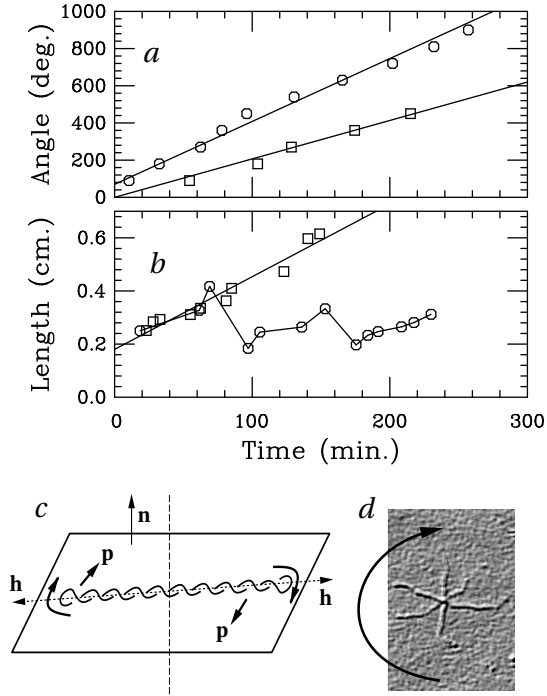


Figure 4.3: Pivoting and fiber growth. (a) uniform rotational motion of left (squares) and right-handed (circles) fibers, and (b) their length evolution, showing several folding events for the RH case. (c) symmetry argument for angular direction of pivoting, with  $\mathbf{n}$  the surface normal,  $\mathbf{h}$  the helicity vectors (lying in the plane, along the plectoneme axis), and  $\mathbf{p}$  the resultant pivoting forces, also in the plane. (d) composite image from above showing pivoting around  $\mathbf{n}$ .

the power generated by a 1 micron spherical bacterium swimming at 10 microns/sec is about 500 nW/cm<sup>3</sup>.

### 4.3 Measurement of the Bending Modulus for *B. subtilis*

Macrofiber self-assembly and the unique motions described here are made possible by the elastic nature of *B. subtilis* cells, that is the material properties of peptidoglycan. This is the “working fluid” of the elastic engine, undergoing repeated elongation and buckling (supercoiling). Even its most basic material properties have not been determined in any direct manner, although studies of large man-made aggregate structures called bacterial thread give estimates of the Young’s modulus [89], which ultimately sets the scale for the propulsive forces. We have determined the bending modulus of single cell filaments from their relaxation [12] after deformation by an optical trap, constructed [90] from a

400 mW NdYVO<sub>4</sub> diode laser (1.064  $\mu\text{m}$ ) (SantaFe Lasers), telescopic beam expansion, motorized steering lenses under computer control (LabView, National Instruments), and a Nikon Diaphot 300 inverted microscope with an oil-immersion plan-apo 100 $\times$  (N.A. 1.4) objective. To increase trapping strength over that achievable with bare filaments, 2  $\mu\text{m}$  diameter latex beads (Ernest F. Fullam) were attached to the filament tip after incubation for 10 minutes in a 0.01 M solution of polylysine (Sigma) and several cycles of rinsing. Attachment was achieved by moving a trapped bead into contact with the filament, which was then bent by steering the trap; when the elastic restoring force of the filament exceeded the trapping force the bead-filament assembly escaped the trap and relaxed. Movies of the bead motion were analyzed using locally-written centroid-tracking software based on a standard algorithm [91].

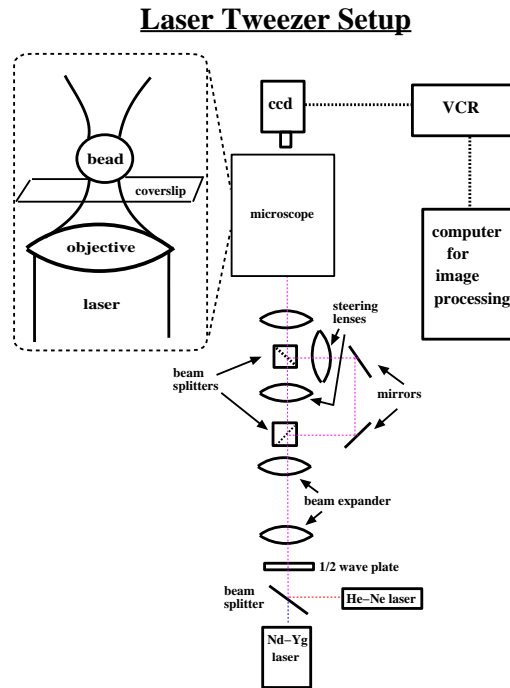


Figure 4.4: Schematic of the setup of the optical trapping system. Note: diagram is not drawn to scale.

The relaxation of the filament tip position  $h(t)$  is of the form  $h_0 \exp(-\sigma t)$ , where  $\sigma = Ak^4/\zeta_{\perp}$ , where  $A$  is the single-filament bending modulus and  $k$  is the first allowed

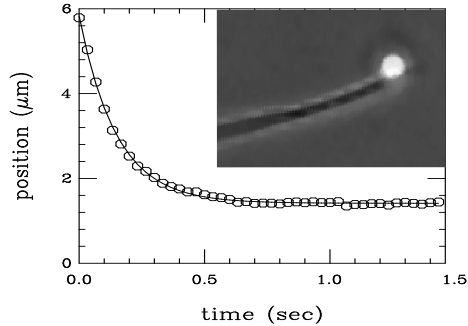


Figure 4.5: Exponential relaxation of a bead attached to a fiber tip, following displacement by an optical trap. Inset shows a  $2 \mu\text{m}$  bead attached to a filament.

wavenumber associated with clamped-free boundary conditions for an elastic filament [12]<sup>2</sup>. Fig. 4.5 shows a typical relaxation curve and its fit to this functional form. From tens of runs on filaments of lengths from  $10 - 50 \mu\text{m}$ , we find  $A \simeq (1.6 \pm 0.6) \times 10^{-12}$  erg-cm. Assigning a persistence length by the relation  $A = k_B T L_p$  we find  $L_p \sim 40 \text{ cm}$ , almost two orders of magnitude larger than that of microtubules [92]. Using  $A$  to estimate the Young's modulus under the simplifying assumption that the stiffness is determined by the thin cell wall (with  $A \simeq \pi a^3 t E$ , with  $t \simeq 25 \text{ nm}$ ) we obtain  $E \sim 0.005 \text{ GPa}$ , quite similar to that of rubber and remarkably close to that found earlier [89].

This single-filament bending modulus can be compared to that inferred from the torque estimates above on macrofibers. If we assume that the torque comes from twist built up in the fiber, then  $\tau_{\text{twist}} \sim C_m \Omega$  where  $C_m$  is the twist elastic modulus of the macrofiber and  $\Omega$  the twist density at the fulcrum. To execute the given motion, the twist must be greater than that needed to cause buckling. Elasticity theory [93] yields the result that buckling occurs when  $(C_m/A_m)\Omega L \approx 10$ . Setting the twist torque equal to the torque necessary to oppose viscous drag and gravity yields  $C_m \sim \tau L/10 \sim 10^{-7}$  erg-cm, fully five orders of magnitude larger than the single filament bending modulus. Assuming, as with most materials, that the bend and twist moduli are comparable, and further invoking the expected scaling of moduli with (radius)<sup>4</sup> shows rough consistency between the filament and fiber data. Clearly, quantitative force measurements on macrofibers are needed, perhaps achievable using mechanical micromanipulation techniques such as

<sup>2</sup>The attached bead does change the boundary conditions some. For a better description of this effect see Appendix K

deflection of needles of known compliance.

The macrofiber elastic engine transduces forces derived from cell growth into motions that accomplish three tasks: assembly of the multicellular fiber form, translational movement over a surface, and the pulling together of objects attached to a fiber's ends. The physics upon which the macrofiber engine operates should be applicable to other biological systems at scales ranging from molecular to multicellular dependent upon the elastic properties of the twisting filament and the environment within which it operates. Further measurements of forces and dynamics are clearly called for in the effort to formulate a more complete picture of this elastic engine.

## Chapter 5

### Conclusions

Through the study of a novel problem involving the forced rotational dynamics of an elastic filament in a viscous environment, a new understanding of the geometrical coupling between twisting and writhing motions was observed. This problem utilized a three dimensional dynamical picture of elasto-hydrodynamics and showed a bifurcation between pure axial rotation and steady state crankshafting motions brought about by the interplay of (i) twist injection, (ii) twist diffusion, and (iii) writhing motions. For the first time, the twist/bend coupling was shown to act as a sink or source for twist. This new understanding can hopefully shed light on some of the interesting dynamical problems that are encountered in the motions of growing bacterial macrofibers as well as in the chirality inversions that are seen in bacterial flagella.

To begin to quantify the forces that are generated in growing *B. subtilis* bacterial macrofibers, we studied the dynamics that occur when a fiber is brought close to a surface. A number of unique chiral motions are observed: rolling, where a macrofiber rotates about its own axis, and pivoting, where the fiber pivots and steps about a fulcrum situated roughly halfway along the length of the fiber. Both of these motions were observed to depend on the internal chirality of the macrofiber. Through calculations based on the drag experienced by the pivoting fiber, estimates of the power generated by the elastic engine driven by growth were possible. To complete the picture of an elastic engine within the cell wall, material parameters that relate to the stiffness and elasticity of the cell are necessary. By using a laser trapping system, we were able to measure the bending modulus of a single filament of *B. subtilis*. Assuming that the elasticity predominantly comes from the cell wall material, we could then estimate the Young's modulus for the cell wall. This was found to be around 5.0 MPa, comparable to that of rubber. These quantitative measurements on bacterial fibers can begin to shed light on the important material parameters for this system and will hopefully lead to a way to discriminate between different proposed models governing the mechanism behind macrofiber formation.

Bacterial flagella are seen to exist in a number of different chiral states. However, no theoretical models have been proposed that take into account the stability of these secondary structures. We proposed the simplest model that can account for some of the dynamic phenomena that are observed in bacterial flagella: bistability of the twist energy functional. We then showed how this twist functional can be incorporated into a totally intrinsic elastohydrodynamic model with which quantitative dimensional arguments can be made that roughly agree with what is seen in experiments. Also, a general formalism was established that can be used to derive intrinsic equations of motion for any filament given the energy and a dynamical statement.

Though our work has led to a better understanding of the viscous dynamics of biological elastic filaments and has also been the first to deal with problems involving twist in the elastohydrodynamic context, a great deal of work, both theoretical and experimental, still remains to be done. To be able to determine the true mechanism behind the formation of bacterial macrofibers the twist modulus must still be measured. Optical trapping methods will most likely not be able to make this measurement. However, magnetic tweezers, which utilize beads with a fixed dipole moment, are now available and could be the perfect apparatus for measuring this value. It is also important to test the dynamical behavior of *B. subtilis* as it may not be purely elastohydrodynamic. Memory effects as new cell wall material is incorporated could lead to some of the phenomena that are seen in experiments, especially the “relaxation” motions that are observed when lysozyme or autolysin are added to the growth medium. One method to test the dynamic behavior would be to see if the relaxation time scales with the length as is predicted by elastohydrodynamics. Some experiments have already been done to test this and show rough agreement with what is predicted, but further experiments are still needed. To test if there are memory or plasticity effects in the cell wall, an experiment where a fiber is bent and held in place for a given amount of time and then released would show if the fiber remains in its new conformation or relaxes back to its original state. Measurements of how viscosity effects the buckling length are also necessary to determine whether twisting stresses or growth induced tension is the predominant buckling factor.

The greatest test of the bistability model for bacterial flagella could be measurements with imposed static forces and torques. These situations need to be explored both experimentally and as well our model needs to be used to produce theoretical predictions for

what might be seen in an experiment. Torque experiments, especially, should provide a view as to the energy landscape for the twist potential for bacterial flagella. As well, it is shown<sup>1</sup> that differences in the force/extension curves should deviate for a bistable helix.

A good theoretical model for plectoneme formation in *B. subtilis* is still lacking. Coupling growth to the elastohydrodynamics involving twist could at least provide a better way to test models for growth induced twisting stresses. With knowledge of the bending and twisting moduli, quantitative comparisons of different models will be able to guide research into a microscopic model for cell wall material inclusion, providing a better picture of bacterial growth and an understanding of the physics that leads to the interesting dynamics and patterns that are seen in these fibers.

---

<sup>1</sup>See Appendix J



## Appendix A

### Variations in $\vec{\Omega}$ and the basis vectors

The shape and twist of an elastic filament can be completely described by the material frame, an orthonormal triad  $\{\hat{\mathbf{e}}_1, \hat{\mathbf{e}}_2, \hat{\mathbf{e}}_3\}$ , with  $\hat{\mathbf{e}}_3$  the tangent,  $\hat{\mathbf{e}}_1$  a unit vector pointing from the filament axis to a fictitious painted line on the filament surface, and  $\hat{\mathbf{e}}_2 = \hat{\mathbf{e}}_3 \times \hat{\mathbf{e}}_1$ . The rotation rate of these vectors is described by  $\mathbf{\Omega} = \Omega_1 \hat{\mathbf{e}}_1 + \Omega_2 \hat{\mathbf{e}}_2 + \Omega_3 \hat{\mathbf{e}}_3$  with

$$\partial_s \hat{\mathbf{e}}_i = \mathbf{\Omega} \times \hat{\mathbf{e}}_i. \quad (\text{A.1})$$

With this relation, it is possible to calculate how variations in the position vector,  $\delta \mathbf{r}$ , and in the rotation angle about the tangent vector,  $\delta \chi = \hat{\mathbf{e}}_2 \cdot \delta \hat{\mathbf{e}}_1$ , affect  $\mathbf{\Omega}$  and the basis vectors. From the above relation, it can be shown that

$$\Omega_j = \hat{\mathbf{e}}_i \cdot \partial_s \hat{\mathbf{e}}_k \quad (\text{A.2})$$

for all cyclic permutations of the indices. Variations in  $\hat{\mathbf{e}}_3$  are found from

$$\begin{aligned} \delta \hat{\mathbf{e}}_3 &= \delta \mathbf{r}_s \\ &= -(\hat{\mathbf{e}}_3 \cdot (\delta \mathbf{r})_s) \mathbf{r}_s + (\delta \mathbf{r})_s \end{aligned} \quad (\text{A.3})$$

where it has been used that  $\delta \partial_s = \partial_s \delta - (\hat{\mathbf{e}}_3 \cdot (\delta \mathbf{r})_s)$ . Since the basis vectors are unit vectors, the tangential components of the variations in  $\hat{\mathbf{e}}_1$  and  $\hat{\mathbf{e}}_2$  are set by  $(\delta \hat{\mathbf{e}}_i) \cdot \hat{\mathbf{e}}_3 = -\hat{\mathbf{e}}_i \cdot (\delta \hat{\mathbf{e}}_3)$ . The other free component is set by our definition of  $\delta \chi$ . Therefore, the variations are

$$\delta \hat{\mathbf{e}}_1 = (\delta \chi) \hat{\mathbf{e}}_2 + (\hat{\mathbf{e}}_1 \cdot (\delta \mathbf{r})_s) \hat{\mathbf{e}}_3 \quad (\text{A.4})$$

$$\delta \hat{\mathbf{e}}_2 = -(\delta \chi) \hat{\mathbf{e}}_1 + (\hat{\mathbf{e}}_2 \cdot (\delta \mathbf{r})_s) \hat{\mathbf{e}}_3 \quad (\text{A.5})$$

Using [A.2,A.3,A.4,A.5], it can be shown that variations in  $\mathbf{\Omega}$  are given by

$$\delta \Omega_1 = (\delta \chi) \Omega_2 - 2\Omega_1 (\hat{\mathbf{e}}_3 \cdot (\delta \mathbf{r})_s) - \hat{\mathbf{e}}_2 \cdot (\delta \mathbf{r})_{ss} \quad (\text{A.6})$$

$$\delta \Omega_2 = -(\delta \chi) \Omega_1 - 2\Omega_2 (\hat{\mathbf{e}}_3 \cdot (\delta \mathbf{r})_s) + \hat{\mathbf{e}}_1 \cdot (\delta \mathbf{r})_{ss} \quad (\text{A.7})$$

$$\delta \Omega_3 = (\delta \chi)_s + (\mathbf{g} - \Omega_3 \hat{\mathbf{e}}_3) \cdot \delta \mathbf{r}_s \quad (\text{A.8})$$

with  $\mathbf{g} = \Omega_1 \hat{\mathbf{e}}_1 + \Omega_2 \hat{\mathbf{e}}_2 = \mathbf{r}_s \times \mathbf{r}_{ss}$ .

## Appendix B

### Derivation of the extrinsic force and writhing terms

An elastic filament whose energy is

$$\mathcal{E} = \int_0^L ds \left( \frac{A}{2} \kappa^2 + \frac{C}{2} \Omega^2 - \Lambda \right), \quad (\text{B.1})$$

with  $\kappa = (\mathbf{r}_{ss} \cdot \mathbf{r}_{ss})^{\frac{1}{2}}$  the curvature,  $\Omega = \Omega_3$  the twist density,  $\Lambda$  is the Lagrange multiplier that enforces local inextensibility, has a force per length given by  $\mathbf{f} = -\delta\mathcal{E}/\delta\mathbf{r}$ . Using the results from Appendix A, and  $\delta ds = (\hat{\mathbf{e}}_3 \cdot (\delta\mathbf{r})_s) ds$ , the variation in the energy can be written as:

$$\delta\mathcal{E} = \int_0^L ds (\mathbf{A}\mathbf{r}_{ss} \cdot (\delta\mathbf{r})_{ss} + C\Omega ((\delta\chi)_s + \mathbf{g} \cdot (\delta\mathbf{r})_s) - \Lambda(\hat{\mathbf{e}}_3 \cdot (\delta\mathbf{r})_s)) \quad (\text{B.2})$$

where  $\mathbf{g} = \Omega_1 \hat{\mathbf{e}}_1 + \Omega_2 \hat{\mathbf{e}}_2 = (\mathbf{r}_s \times \mathbf{r}_{ss})$  and a factor of  $\frac{1}{2}(C\Omega^2 + 3A\kappa^2)$  has been absorbed into  $\Lambda$ .<sup>1</sup>

To compute the force per length, the variational derivative of the energy is taken with respect to  $\delta\mathbf{r}$ , with  $\delta\chi = 0$ . This is easily accomplished with the above result for the variation in the energy,

$$\begin{aligned} \mathbf{f} &= -\partial_{ss}(\mathbf{A}\mathbf{r}_{ss}) + \partial_s(C\Omega(\mathbf{r}_s \times \mathbf{r}_{ss}) - \Lambda\mathbf{r}_s) \\ &= -\mathbf{A}\mathbf{r}_{4s} + C[\Omega(\mathbf{r}_s \times \mathbf{r}_{ss})]_s - \Lambda_s\mathbf{r}_s - \Lambda\mathbf{r}_{ss} \end{aligned} \quad (\text{B.3})$$

The writhetracking piece in the  $\Omega$  equation<sup>2</sup> is  $\mathbf{r}_s \times \mathbf{r}_{ss} \cdot (\mathbf{f}_\perp)_s$ , where  $\mathbf{f}_\perp = \mathbf{f} - (\mathbf{f} \cdot \mathbf{r}_s)\mathbf{r}_s$ . Calculating the derivative of  $\mathbf{f}_\perp$  gives:

$$\begin{aligned} (\mathbf{f}_\perp)_s &= \partial_s [-\mathbf{A}\mathbf{r}_{4s} + C[\Omega(\mathbf{r}_s \times \mathbf{r}_{ss})]_s - \Lambda\mathbf{r}_{ss} + A(\mathbf{r}_{4s} \cdot \mathbf{r}_s)\mathbf{r}_s] \\ &= -\mathbf{A}\mathbf{r}_{5s} + C[\Omega_{ss}(\mathbf{r}_s \times \mathbf{r}_{ss}) + 2\Omega_s(\mathbf{r}_s \times \mathbf{r}_{3s}) + \Omega\partial_s(\mathbf{r}_s \times \mathbf{r}_{3s})] \\ &\quad - \Lambda_s\mathbf{r}_{ss} - \Lambda\mathbf{r}_{3s} + A(\mathbf{r}_{5s} \cdot \mathbf{r}_s)\mathbf{r}_s + A(\mathbf{r}_{4s} \cdot \mathbf{r}_{ss})\mathbf{r}_s + A(\mathbf{r}_{4s} \cdot \mathbf{r}_s)\mathbf{r}_{ss} \end{aligned} \quad (\text{B.4})$$

<sup>1</sup>Any term of the form  $f(s)\hat{\mathbf{e}}_3 \cdot (\delta\mathbf{r})_s$ , where  $f(s)$  is an arbitrary function, can be absorbed into the Lagrange multiplier.

<sup>2</sup>See Appendix G

Thus,

$$\begin{aligned}
(\mathbf{r}_s \times \mathbf{r}_{ss}) \cdot \mathbf{f}_s &= -A\mathbf{r}_{5s} \cdot (\mathbf{r}_s \times \mathbf{r}_{ss}) + C[\Omega_{ss}|\mathbf{r}_s \times \mathbf{r}_{ss}|^2 + \Omega_s(\mathbf{r}_{3s} \cdot \mathbf{r}_{ss}) \\
&\quad - \Omega((\mathbf{r}_{ss} \cdot \mathbf{r}_{4s} - (\mathbf{r}_{ss} \cdot \mathbf{r}_{ss})^2)] - \Lambda\mathbf{r}_{3s} \cdot (\mathbf{r}_s \times \mathbf{r}_{ss})
\end{aligned} \tag{B.5}$$

Utilizing the Frenet-Serret equations

$$\mathbf{r}_{ss} = \kappa \hat{\mathbf{n}} \tag{B.6}$$

$$\hat{\mathbf{n}}_s = -\kappa \mathbf{r}_s + \tau \hat{\mathbf{b}} \tag{B.7}$$

$$\hat{\mathbf{b}}_s = -\tau \hat{\mathbf{n}}, \tag{B.8}$$

where  $\hat{\mathbf{n}} = \mathbf{r}_{ss}/\kappa$  and  $\hat{\mathbf{b}} = \mathbf{r}_s \times \hat{\mathbf{n}}$ , to rewrite the writhetracking piece in terms of the curvature and the torsion,  $\tau$ , leads to

$$(\mathbf{r}_s \times \mathbf{r}_{ss}) \cdot \mathbf{f}_s = -A[3\kappa(\kappa_s\tau)_s + \kappa^2(\tau_{ss} - \tau^3 - \kappa^2\tau)] + C[\kappa(\Omega\kappa)_{ss} - \Omega\kappa^2\tau^2] + \Lambda\kappa^2\tau. \tag{B.9}$$

This equation is zero unless  $\mathbf{f} \neq 0$  and the filament is either twisted ( $\Omega \neq 0$ ) or bent out of the plane ( $\tau \neq 0$ ).

## Appendix C

### Linear Analysis of the Twirl-to-Whirl Instability

For the linear stability analysis we will assume that,  $\xi(s, t) = \xi(s)e^{(\sigma+i\chi)t}$ . Plugging this into the linear equation turns the PDE into an ODE given by:

$$(\sigma + i\chi)\xi = -\xi_{4s} + i\Gamma\alpha[(s-1)\xi_{ss}]_s \quad (\text{C.1})$$

where  $\alpha$  is the rescaled rotational turning velocity.

This is a non-trivial equation. However, some insight into the solution can be gained by looking at the small  $\alpha$  limit. In the case when  $\alpha = 0$ , this reduces to:

$$(\sigma + i\chi)\xi = -\xi_{4s} \quad (\text{C.2})$$

The solution to this is just:

$$\xi(s) = \sum_n (a_n \sin(k_n s) + b_n \cos(k_n s) + c_n \sinh(k_n s) + d_n \cosh(k_n s)) \quad (\text{C.3})$$

where  $a, b, c, d$  and  $k$  are constants set by the boundary conditions.

If we use the boundary conditions that relate to having the filament clamped at  $s = 0$ , and free at  $s = L$ , this corresponds to:  $\xi(0) = \xi_s(0) = 0$  and  $\xi_{ss}(L) = \xi_{3s}(L) = 0$ . It can then be calculated that:

$$\xi = \sum_n \left( a_n (\cos(k_n s) - \cosh(k_n s)) + \frac{\sin(k_n L) - \sinh(k_n L)}{\cos(k_n L) + \cosh(k_n L)} (\sin(k_n s) - \sinh(k_n s)) \right) \quad (\text{C.4})$$

where the  $k_n$ 's satisfy the equation:

$$\cos(k_n L) \cosh(k_n L) = -1 \quad (\text{C.5})$$

This implies that the growth rate for the first mode is given by  $\sigma = (1.875/L)^4$ .

If we now assume that  $\alpha$  is small, we can treat the term  $i\Gamma\alpha((s-1)\xi_{ss})_s$  as a perturbation and find the order  $\alpha$  correction to the growth rate. If we think of this quantum mechanically, we can rewrite the equation as:

$$(\text{H} + \text{V})\xi = \lambda\xi \quad (\text{C.6})$$

where  $H = -\partial_s^4$ ,  $V = i\alpha\partial_s(s\partial_s^2)$ , and  $\lambda = \sigma + i\chi$ . Since we are in the realm of small  $\alpha$ ,  $V$  is a perturbation and we can expand  $\lambda$  in powers of  $\alpha$  as:

$$\lambda = \lambda^{(0)} + \alpha\lambda^{(1)} + \mathcal{O}(\alpha^2) \quad (\text{C.7})$$

Since  $H$  is hermitian,  $\lambda^{(0)}$  will be real. This means that  $\chi^{(0)} = 0$ .

Rewriting  $\xi$  as a sum over the different modes as:

$$\xi = \sum_n a_n \phi_n \quad (\text{C.8})$$

yields

$$H\xi = \sum_n \sigma_n^{(0)} a_n \phi_n \quad (\text{C.9})$$

If we choose to find the first order correction to the first mode, we can write  $\xi$  as an expansion in  $\alpha$  as:

$$\xi = \phi_1 + \alpha \sum_{n \neq 1} a_n \phi_n + \mathcal{O}(\alpha^2) \quad (\text{C.10})$$

And therefore, the first order correction can be found to be equal to:

$$\lambda^{(1)} = \langle \phi_1 | V \phi_1 \rangle / \langle \phi_1 | \phi_1 \rangle \quad (\text{C.11})$$

Using the form for  $\xi$  found above with  $L = 1$ , and  $k_1 = 1.875$ , this integral was found to be equal to  $i2.3239$ . Therefore,  $\chi^{(1)} = 2.32\alpha$  and  $\sigma^{(1)} = 0$ . This implies that the growth rates,  $\sigma^{(n)}$ , to a first approximation, vary quadratically in the turning frequency.

## Appendix D

### Numerical Methods for Twirling and Whirling

To analyze the dynamical behavior of an initially straight rod, immersed in a viscous fluid, that is turned at one end with a rotational frequency of  $\omega$ , we need to solve a set of coupled PDE's that govern the position and twist of the filament. Those PDE's are

$$\zeta_{\perp} \mathbf{r}_t = \mathbf{f} + \left( \frac{\zeta_{\perp} - \zeta_{\parallel}}{\zeta_{\parallel}} \right) (\mathbf{f} \cdot \mathbf{r}_s) \mathbf{r}_s \quad (\text{D.1})$$

$$\Omega_t = \frac{C}{\zeta_r} \Omega_{ss} + \frac{1}{\zeta_{\perp}} \mathbf{r}_s \times \mathbf{r}_{ss} \cdot \mathbf{f}_s, \quad (\text{D.2})$$

with the force per length,<sup>1</sup>

$$\mathbf{f} = -A \mathbf{r}_{4s} + C [\Omega(\mathbf{r}_s \times \mathbf{r}_{ss})]_s - (\Lambda \mathbf{r}_s)_s. \quad (\text{D.3})$$

These equations can be nondimensionalized by choosing the following rescalings:

$$\begin{aligned} \tilde{\mathbf{r}} &= \mathbf{r}/L, & \tilde{\Omega} &= \Omega L, \\ \tilde{s} &= s/L, & \tilde{t} &= (A/\zeta_{\perp} L^4) t, \\ \tilde{\mathbf{f}} &= \mathbf{f} L^3/A, & \tilde{\Lambda} &= \Lambda L^2/A. \end{aligned}$$

The dimensionless equations are now:

$$\mathbf{r}_t = \mathbf{f} + \left( \frac{\zeta_{\perp} - \zeta_{\parallel}}{\zeta_{\parallel}} \right) (\mathbf{f} \cdot \mathbf{r}_s) \mathbf{r}_s \quad (\text{D.4})$$

$$\Omega_t = \frac{\Gamma}{\epsilon^2} \Omega_{ss} + \mathbf{r}_s \times \mathbf{r}_{ss} \cdot \mathbf{f}_s, \quad (\text{D.5})$$

$$\mathbf{f} = -\mathbf{r}_{4s} + \Gamma [\Omega(\mathbf{r}_s \times \mathbf{r}_{ss})]_s - (\Lambda \mathbf{r}_s)_s. \quad (\text{D.6})$$

where  $\Gamma = C/A$ ,  $\epsilon^2 = \zeta_{\perp} L^2/\zeta_r$ , and the tildes have been dropped for simplicity. We are interested in studying systems where the filament can not stretch. This restriction implies that  $\mathbf{r}_{t,s} \cdot \mathbf{r}_s = 0$ . From this it can be shown that  $(1 - \zeta_{\parallel}/\zeta_{\perp})(\mathbf{r}_{ss} \cdot \mathbf{f}) + (\mathbf{r}_s \cdot \mathbf{f}) = \frac{1}{2}(\mathbf{r}_{ss} \cdot \mathbf{f}) + (\mathbf{r}_s \cdot \mathbf{f}) = 0$ , which closes the system of equations by providing a condition on  $\Lambda$ .

If we are interested in the dynamics of the filament shortly after the filament buckles, we can expand the position about the straight state by defining  $\mathbf{r}(s, t) = [X(s, t), Y(s, t), s - \delta(s, t)]$ , where the deviations  $X$ ,  $Y$ , and  $\delta$  are presumed to be small. The unitarity of the tangent vector fixes  $\delta_s \simeq \frac{1}{2}(X_s^2 + Y_s^2)$ , implying that  $\delta$  is a second order quantity. To obtain the weakly nonlinear expansion of these PDE's, we need to know

$$\mathbf{r}_s \times \mathbf{r}_{ss} = [X_s, Y_s, 1 - \delta_s] \times [X_{ss}, Y_{ss}, -\delta_{ss}] \quad (\text{D.7})$$

$$= [-Y_s \delta_{ss} - Y_{ss}(1 - \delta_s), X_{ss}(1 - \delta_s) + X_s \delta_{ss}, X_s Y_{ss} - Y_s X_{ss}] \quad (\text{D.8})$$

$$\approx [-Y_{ss}, X_{ss}, X_s Y_{ss} - Y_s X_{ss}] \quad (\text{D.9})$$

with the last line expanded to second order. By defining  $\xi = (X + iY)$ , the dynamical equations can be written out to second order as

$$\begin{aligned} \xi_t &= -\xi_{4s} - (\Lambda \xi)_s + i\Gamma [\Omega (\xi_{ss}(1 - \delta_s) + \delta_{ss} \xi_s)]_s \\ &\quad - \left[ \frac{1}{2} (\xi_{4s}^* \xi_s + \xi_{4s} \xi_s^*) + \Lambda_s \right] \xi_s \\ \Omega_t &= \frac{\Gamma}{\epsilon^2} \Omega_{ss} + \frac{1}{2} [i (\xi_{5s}^* \xi_{ss} - \xi_{5s} \xi_{ss}^*) \\ &\quad + \Gamma ((\Omega \xi_{ss}^*)_{ss} \xi_{ss} + (\Omega \xi_{ss})_{ss} \xi_{ss}^*)] , \end{aligned} \quad (\text{D.10})$$

and the inextensibility constraint sets  $\Lambda$  as

$$\left( \Lambda - \frac{3}{2} |\xi_{ss}|^2 \right)_{ss} = \frac{1}{2} (\mathcal{R}e(\xi_{4s} \xi_{ss}^*) + i\Gamma \Omega \mathcal{I}m(\xi_{3s} \xi_{ss}^*)).$$

To solve these equations numerically, we chose to use a pseudospectral method [61]. This method utilizes the stability of a Fourier analysis by time stepping the linear part of the PDE's spectrally. The nonlinear terms are calculated from the previous timestep, transformed and used to timestep the full equation in a spectral way. This amounts to having the linear terms at the proper time and the nonlinear terms one time step behind. This method allows quicker calculation time as the time step can be made larger than is normally possible with a pure finite difference method.

The linear part of the  $\xi$  equation is fourth order in spatial derivatives. This implies that the proper equations to use are biharmonic functions. A complete set of equations can be generated by combining cos, sin, cosh, and sinh terms. For the problem of a filament rotated at one end, we assume that the boundary conditions are such that

the rotated end is clamped ( $\xi(0) = \xi_s(0) = 0$ ), and the other end is free (no torques ( $\xi_{ss}(L) = 0$ ), no forces ( $\xi_{3s}(L) = 0$ )). Under these conditions the complete set of equations is found as C.4. These functions are used to transform the nonlinear pieces spectrally.

The linear part of the  $\Omega$  equation is second order in spatial derivatives. This means that regular Fourier functions may be used to transform the equations. The boundary conditions on  $\Omega$  are found from the fact that the one end is rotated. Torque balance at that end gives that  $\zeta_r \omega_0 = C \Omega_s(0)$ . At the free end,  $\Omega(L) = 0$ . This enables us to solve the  $\Omega$  equation in the absence of the nonlinear terms which couple twist and bend motions. The solution is that  $\Omega$  varies linearly with the arclength,

$$\Omega^0 = (\zeta_r \omega_0 / C)(s - L) \tag{D.11}$$

If we define  $\Omega = \Omega^0 + \lambda$ , instead of solving for  $\Omega$ , we solve for  $\lambda$ . This removes the difficulty of having to enforce the boundary condition on  $\Omega_s$  at the rotated end. The boundary conditions become  $\lambda(0) = \lambda(L) = 0$ , and sine functions are used to do the Fourier analysis of  $\lambda$ .



## Appendix E

### $\Psi$ to Real Space Conversion

In this appendix, I describe the procedure that is used to transform the complex, intrinsic  $\Psi$  representation for a space curve into the real space representation.

A curve is described by the real space vector,  $\mathbf{r}$ , which is parameterized by the distance along the curve,  $s$ , the arclength. The tangent vector is  $\mathbf{r}_s$ . If the tangent vector of the curve is known, the curve can be reconstructed by assuming an arbitrary starting position,  $\mathbf{r}^0$ , and integrating.

The curve can also be described by an intrinsic  $\Psi$  representation (See Eq. 3.4). The function  $\Psi$  governs how the tangent,  $\hat{\mathbf{e}}_3$ , and the two complex vectors normal to  $\hat{\mathbf{e}}_3$ ,  $\epsilon$  and  $\epsilon^*$ , evolve in space,

$$\partial_s \hat{\mathbf{e}}_3 = \Re(\Psi \epsilon^*) , \quad (\text{E.1})$$

$$\partial_s \epsilon = -\Psi \hat{\mathbf{e}}_3 . \quad (\text{E.2})$$

To reconstruct the curve using this representation, these equation need to be integrated to find the tangent vector, and then the tangent vector is integrated to give back the curve. I will assume that the function  $\Psi$  is known. Since this representation is totally intrinsic, all information relating to the absolute position of the filament is lacking. Reconstruction of the curve will only provide a relative positioning of the curve. However, the actual shape will be consistent. To continue, the initial directions of the triad are set as  $(\epsilon^0, \epsilon^{*0}, \hat{\mathbf{e}}_3^0)$ , where we require that these form an orthonormal triad. These equations are then integrated as

$$\hat{\mathbf{e}}_3 = \hat{\mathbf{e}}_3^0 + \int_0^s (\Psi_R \epsilon_R^* + \Psi_I \epsilon_I^* + \Psi_R^* \epsilon_R + \Psi_I^* \epsilon_I) ds' \quad (\text{E.3})$$

$$\epsilon_R = \epsilon_R - \int_0^s \Psi_R \hat{\mathbf{e}}_3 ds' \quad (\text{E.4})$$

$$\epsilon_I = \epsilon_I - \int_0^s \Psi_I \hat{\mathbf{e}}_3 ds' \quad (\text{E.5})$$

$$\epsilon_R^* = \epsilon_R^* - \int_0^s \Psi_R^* \hat{\mathbf{e}}_3 ds' \quad (\text{E.6})$$

$$\epsilon_I^* = \epsilon_I^* - \int_0^s \Psi_I^* \hat{\mathbf{e}}_3 ds' \quad (\text{E.7})$$

where the subscripts  $R$  and  $I$  stand for the real and imaginary parts, respectively.

## Appendix F

### Growth Induced Buckling

A straight growing filament will feel a spatially dependent tension along its length due to drag as the filament extends. Since *B. subtilis* fibers grow exponentially in time, the velocity at the end of the fiber will get exponentially faster. At some point, the drag due to this velocity will create a tension great enough to buckle the filament. Using dimensional analysis, the drag per length will be equal to  $\zeta_{\parallel}v \sim \zeta_{\parallel}\sigma L$ , where  $\zeta_{\parallel}$  is the drag coefficient for motions parallel to the long axis of the fiber,  $v$  is the velocity at the end of the fiber,  $\sigma$  is the growth rate, and  $L$  is the length of the fiber. Therefore, an estimate for the magnitude of the tension in the fiber is  $\sim \zeta_{\parallel}\sigma L^2$ . Setting this equal to the force required to buckle the filament,  $A/L^2$  gives the bending modulus,  $A$ , for which a fiber of length,  $L$  and growth rate  $\sigma$  will buckle.

$$A = \zeta_{\parallel}\sigma L^4 \tag{F.1}$$

For FJ7 right-handed structures, with a growth rate of  $1.5 \times 10^{-4}$ s and a buckling length of  $1.7 \times 10^{-2}$ cm, this gives a bending modulus of  $1.3 \times 10^{-13}$ erg.cm, a factor of 10 off from what was found experimentally, but close enough to warrant a better analysis.

The equation of motion is

$$\zeta_{\parallel}\hat{\mathbf{t}}\hat{\mathbf{t}} \cdot \mathbf{r}_t + \zeta_{\perp}(\mathbf{I} - \hat{\mathbf{t}}\hat{\mathbf{t}}) \cdot \mathbf{r}_t = \mathbf{f}, \tag{F.2}$$

and to linear order  $\mathbf{f} = -A\mathbf{r}_{4s} - \partial_s(\Lambda\mathbf{r}_s)$ , where  $\Lambda$  is a Lagrange multiplier that enforces the growth condition. Since the fiber is growing exponentially along its long axis,  $\mathbf{r}_t = \sigma s\mathbf{r}_s$ , where  $s = s_0e^{\sigma t}$  is the arclength. Combining this equation with the dynamical equation sets the derivative of the Lagrange multiplier as

$$\Lambda_s = -\zeta_{\parallel}\sigma s \tag{F.3}$$

where it is assumed that  $s = 0$  is the middle of the filament. Since the ends of the filament are considered to be free, there can be no force at the ends. This implies that

the boundary conditions are that  $\Lambda$  at the ends is zero, and therefore,  $\Lambda = \frac{1}{2}\zeta_{\parallel}\sigma(\frac{1}{4}L^2 - s^2)$ . The linear dynamical equation for displacements perpendicular to the growing fiber axis can now be written as:

$$\zeta_{\perp}x_t = -Ax_{4s} - \frac{1}{2}\zeta_{\parallel}\sigma\left(\frac{1}{4}L^2 - s^2\right)x_{ss} \quad (\text{F.4})$$

with  $x$  the displacement perpendicular to the original fiber axis. By rescaling the arclength by the length,  $\tilde{s} = s/L$ , and the time as  $\tilde{t} = At/L^4$  gives

$$x_t = -x_{4s} - \alpha\left(\frac{1}{4}L^2 - s^2\right)x_{ss} \quad (\text{F.5})$$

where  $\alpha = \zeta_{\parallel}\sigma L^4/2A$  is the one control parameter. This equation can be solved numerically to find the value of  $\alpha$  where a perturbation goes unstable. This was found to be  $\alpha \approx 93.0$ . This gives that the buckling length for *B. subtilis* is

$$L_b = \left(\frac{186A}{\zeta_{\parallel}\sigma}\right)^{\frac{1}{4}} \quad (\text{F.6})$$

with  $A \sim 10^{-12}\text{erg}\cdot\text{cm}$ ,  $\zeta_{\parallel} \sim 10^{-2}\text{erg}\cdot\text{cm}^{-2}$ , and  $\sigma \sim 10^{-4}$ , this gives  $L_b = 0.1\text{cm}$ . Though this number is a factor of 10 high for FJ7 fibers it is comparable to the buckling length for RHX. Therefore, it may not be the main driving force of buckling, but probably plays a significant role.

## Appendix G

### Derivation of the Dynamic Equations for $\Psi$ and $\Omega$

The material frame basis vectors can vary in both space and time. The equations governing this motion is

$$\partial_s \hat{\mathbf{e}}_i = \boldsymbol{\Omega} \times \hat{\mathbf{e}}_i \quad (\text{G.1})$$

$$\partial_t \hat{\mathbf{e}}_i = \boldsymbol{\omega} \times \hat{\mathbf{e}}_i \quad (\text{G.2})$$

where  $\boldsymbol{\Omega}$  is the previously defined spatial rotation rate of the the basis vectors (See eg. Appendix A), and  $\boldsymbol{\omega}$  is describes the rotation of the basis in time, and, therefore, acts like and angular velocity. If we switch to our complex notation,  $\epsilon = (\hat{\mathbf{e}}_1 + i\hat{\mathbf{e}}_2)e^{i\vartheta}$ , these two equations can be written as

$$\begin{aligned} \partial_s \hat{\mathbf{e}}_3 &= \Re(\Psi \epsilon^*) , & \partial_s \epsilon &= -\Psi \hat{\mathbf{e}}_3 \\ \partial_t \hat{\mathbf{e}}_3 &= \Re(\Pi \epsilon^*) , & \partial_t \epsilon &= -\Pi \hat{\mathbf{e}}_3 + i(\vartheta_t - \omega) , \end{aligned} \quad (\text{G.3})$$

where  $\omega = \omega_3$  has been used to simplify the notation.

The commutator,  $[\partial_t, \partial_s] = \partial_t \partial_s - \partial_s \partial_t = -(\hat{\mathbf{e}}_3 \cdot \mathbf{r}_{t,s}) \partial_s$ , can be used to show that

$$[\partial_t, \partial_s] \epsilon = -(\hat{\mathbf{e}}_3 \cdot \mathbf{r}_{t,s}) \epsilon_s \quad (\text{G.4})$$

$$= (\hat{\mathbf{e}}_3 \cdot \mathbf{r}_{t,s}) \Psi \hat{\mathbf{e}}_3 . \quad (\text{G.5})$$

Looking at the  $\epsilon$  components from this commutator,

$$-\Psi \Pi^* = -\Pi \Psi^* + 2i \partial_s (\vartheta_t - \omega) \quad (\text{G.6})$$

Therefore,

$$(\vartheta_t - \omega) = \int^s \Im(\Pi \Psi^*) ds' \quad (\text{G.7})$$

and

$$\partial_t \epsilon = -\Pi \hat{\mathbf{e}}_3 + i \epsilon \int^s \Im(\Pi \Psi^*) ds' \quad (\text{G.8})$$

Using the definitions for  $\Psi$  and  $\Omega$ ,

$$\Psi = \mathbf{r}_{ss} \cdot \boldsymbol{\epsilon} \quad (\text{G.9})$$

$$\Omega = \hat{\mathbf{e}}_2 \cdot \partial_s \hat{\mathbf{e}}_1, \quad (\text{G.10})$$

it is possible to write the kinematic equations that describe the motion of the filament backbone and twist, respectively. By taking the time derivative of (3.4), we get the kinematic equation governing the backbone conformation.

$$\Psi_t = \partial_t (\mathbf{r}_{ss} \cdot \boldsymbol{\epsilon}) \quad (\text{G.11})$$

$$= \partial_t (\mathbf{r}_{ss}) \cdot \boldsymbol{\epsilon} + \mathbf{r}_{ss} \cdot \partial_t \boldsymbol{\epsilon} \quad (\text{G.12})$$

$$= \partial_s (\hat{\mathbf{e}}_{3,t}) \cdot \boldsymbol{\epsilon} - (\hat{\mathbf{e}}_3 \cdot \mathbf{r}_{t,s}) \mathbf{r}_{ss} \cdot \boldsymbol{\epsilon} + \mathbf{r}_{ss} \cdot (\Pi \hat{\mathbf{e}}_3 + i\boldsymbol{\epsilon} \int^s \Im(\Pi \Psi^*) ds') \quad (\text{G.13})$$

$$= \Pi_s - \Psi \hat{\mathbf{e}}_3 \cdot \mathbf{r}_{t,s} + i\Psi \int^s \Im(\Pi \Psi^*) ds' \quad (\text{G.14})$$

The first term describes how differential rotation rates produce strain, the second term is a coupling between bend and stretching and the third term couples twisting motions with bending.

The kinematic equation for  $\Omega$  is found in the same way.

$$\Omega_t = \partial_t (\hat{\mathbf{e}}_2 \cdot \partial_s \hat{\mathbf{e}}_1) \quad (\text{G.15})$$

$$= \hat{\mathbf{e}}_{2,t} \cdot \partial_s \hat{\mathbf{e}}_1 - \Omega \hat{\mathbf{e}}_3 \cdot \mathbf{r}_{t,s} + \hat{\mathbf{e}}_2 \cdot \partial_s (\hat{\mathbf{e}}_{1,t}) \quad (\text{G.16})$$

$$= (\omega_1 \hat{\mathbf{e}}_3 - \omega_3 \hat{\mathbf{e}}_1) \cdot (\Omega_3 \hat{\mathbf{e}}_2 - \Omega_2 \hat{\mathbf{e}}_3) - \Omega \hat{\mathbf{e}}_3 \cdot \mathbf{r}_{t,s} + \hat{\mathbf{e}}_2 \cdot \partial_s (\omega_3 \hat{\mathbf{e}}_2 - \omega_2 \hat{\mathbf{e}}_3) \quad (\text{G.17})$$

$$= -\omega_1 \Omega_2 - \Omega \hat{\mathbf{e}}_3 \cdot \mathbf{r}_{t,s} + \omega_{3,s} - \omega_2 \hat{\mathbf{e}}_2 \cdot (\Omega_2 \hat{\mathbf{e}}_1 - \Omega_1 \hat{\mathbf{e}}_2) \quad (\text{G.18})$$

$$= \omega_{3,s} - (\hat{\mathbf{e}}_3 \cdot \mathbf{r}_{t,s}) \Omega - \omega_1 \Omega_2 + \omega_2 \Omega_1 \quad (\text{G.19})$$

$$= \omega_s - \Omega \hat{\mathbf{e}}_3 \cdot \mathbf{r}_{t,s} + \Im(\Psi^* \Pi) \quad (\text{G.20})$$

where in the last line  $\omega = \omega_3$  has been used to simplify the notation. The last term in this equation is the coupling between twist and bend. It describes how writhing motions affect the twist in a filament and can act as either a sink or a source for twist. It can be shown that this *writhetracking* piece can be rewritten as  $\Im(\Psi^* \Pi) = (\mathbf{r}_s \times \mathbf{r}_{ss}) \cdot \mathbf{r}_{t,s}$ .

To complete the dynamics, we must think in terms of a Hamiltonian-type dynamics. What we have just derived accounts for the first order position equations from a Hamiltonian system. What we need then is the first order momentum equations. To get these

we must define our dynamics. If we are to explain the overdamped world in which cells live, then we set forces per length proportional to momenta. In our language, the viscous force per length can be related to  $\Pi$  by

$$\mathbf{f} = \zeta \mathbf{r}_t \quad (\text{G.21})$$

$$\mathbf{f}_s = \zeta \mathbf{r}_{t,s} \quad (\text{G.22})$$

$$\mathbf{f}_s = \zeta \mathbf{r}_{s,t} - (\hat{\mathbf{e}}_3 \cdot \mathbf{r}_{t,s}) \mathbf{r}_s \quad (\text{G.23})$$

$$\mathbf{f}_s \cdot \epsilon = \zeta \Pi \quad (\text{G.24})$$

Plugging in this final equation for  $\Pi$  into the kinematic equation for  $\Psi$  gives back the result found in [38].

If we want to do inertial dynamics for the filament, then we would use that  $\rho \mathbf{r}_{tt} = \mathbf{f}$  where  $\rho$  is the mass per length of the filament. Following the same procedure that we just used (but for simplicity using that space and time derivatives commute)

$$\mathbf{f}_s = \rho \mathbf{r}_{tt,s} \quad (\text{G.25})$$

$$= \rho \mathbf{r}_{s,tt} \quad (\text{G.26})$$

$$= \rho \partial_t (\Re(\Pi^* \epsilon)) \quad (\text{G.27})$$

$$= \rho \left( \Re(\Pi_t^* \epsilon) - |\Pi|^2 \hat{\mathbf{e}}_3 + i(\vartheta_t - \omega) \Re(\Pi^* \epsilon) \right) \quad (\text{G.28})$$

$$\mathbf{f}_s \cdot \epsilon = \rho (\Pi_t + i\Pi(\vartheta_t - \omega)) \quad (\text{G.29})$$

$$= \rho \left( \Pi_t + i\Pi \int^s \Im(\Pi \Psi^*) ds' \right) \quad (\text{G.30})$$

Once  $\mathbf{f}$  has been specified, this equation and the kinematic equation for  $\Psi$  finish the  $\Psi$  dynamic equations. To complete the dynamics, similar expressions must be derived for the twist dynamics. In the viscous case, these are  $\zeta_r \omega = m$  where  $m$  is the torque about the tangent vector per unit length and  $\zeta_r$  is the rotational drag coefficient. In the inertial case,  $m = 2I\omega_t$  with  $I$  being the moment of inertia about the tangent vector.

## Appendix H

### Correction to the Block Angle

When dealing with filaments whose unstressed state is straight, it is natural to use the position of the backbone of the filament to describe the conformation (and stresses) in the fiber. One of the most used parameterizations in this description is the Frenet-Serret (F-S) frame, where an orthonormal triad is created using the vectors  $\hat{\mathbf{t}} = \mathbf{r}_s$ ,  $\hat{\mathbf{n}}$ , and  $\hat{\mathbf{b}} = \hat{\mathbf{t}} \times \hat{\mathbf{n}}$ .  $\hat{\mathbf{t}}$  is the tangent vector and the other vectors are defined through the equations:

$$\hat{\mathbf{t}}_s = \kappa \hat{\mathbf{n}} \tag{H.1}$$

$$\hat{\mathbf{n}}_s = -\kappa \hat{\mathbf{t}} + \tau \hat{\mathbf{b}} \tag{H.2}$$

$$\hat{\mathbf{b}}_s = -\tau \hat{\mathbf{n}} \tag{H.3}$$

where  $\kappa$  is the curvature and  $\tau$  is the torsion. However, when the filaments unstressed state is helical, it would seem that the helix axis is just as useful for describing the conformation of the filament as the backbone. In the DNA literature, this is actually the preferred way to describe the shape of the DNA polymer. In DNA, there is a separation of scales that makes this description the most useful. Since the radius of curvature and the pitch are orders of magnitude smaller than the length, most interesting bending stresses occur on scales much larger than the preferred curvature. However, with bacterial flagella, the pitch and radius of curvature are both only an order of magnitude smaller than the length of the filament. This means that there is not the strong separation of length scales that was so useful for DNA. Yet, it still seems that a natural description of the flagella can be made by describing the position of the helical axis. This description will also prove to be useful for describing the Block angle that is seen in bacterial flagella, as well as corrections to this angle from finite width fronts.

To begin to describe the position of a naturally bent filament, it is important to notice that any portion of a bent filament can be described as a piece of a helix with radius



of curvature,  $R = \kappa/(\kappa^2 + \tau^2)$ , and pitch,  $P = 2\pi\tau/(\kappa^2 + \tau^2)$ . Using this F-S type description, we can define the axis of this helical segment by the unit vector:

$$\hat{\mathbf{z}} = \frac{\tau\hat{\mathbf{t}}}{(\kappa^2 + \tau^2)^{\frac{1}{2}}} + \frac{\kappa\hat{\mathbf{b}}}{(\kappa^2 + \tau^2)^{\frac{1}{2}}} \quad (\text{H.4})$$

where  $\hat{\mathbf{t}} = \mathbf{r}_s$  is the tangent vector and  $\hat{\mathbf{b}}$  is the F-S binormal vector. A orthonormal triad can be made by noting that the F-S normal vector,  $\hat{\mathbf{n}}$ , is perpendicular to  $\hat{\mathbf{z}}$ . Therefore, the triad is completed by defining  $\hat{\mathbf{x}} = \hat{\mathbf{n}} \times \hat{\mathbf{z}}$ . The next thing that is needed is to describe the spatial evolution of these vectors.

$$\hat{\mathbf{z}}_s = \partial_s \left( \frac{\tau\hat{\mathbf{t}}}{(\kappa^2 + \tau^2)^{\frac{1}{2}}} + \frac{\kappa\hat{\mathbf{b}}}{(\kappa^2 + \tau^2)^{\frac{1}{2}}} \right) \quad (\text{H.5})$$

$$= (\kappa^2 + \tau^2)^{-\frac{1}{2}}(\tau_s\hat{\mathbf{t}} + \kappa_s\hat{\mathbf{b}}) - (\kappa^2 + \tau^2)^{-\frac{3}{2}}(\tau\hat{\mathbf{t}} + \kappa\hat{\mathbf{b}})(\kappa\kappa_s + \tau\tau_s) \quad (\text{H.6})$$

$$= (\kappa^2 + \tau^2)^{-\frac{3}{2}}(\kappa^2\tau_s\hat{\mathbf{t}} + \tau^2\kappa_s\hat{\mathbf{b}} - \kappa\tau\kappa_s\hat{\mathbf{t}} - \kappa\tau\tau_s\hat{\mathbf{b}}) \quad (\text{H.7})$$

$$= \frac{\kappa\tau_s - \kappa_s\tau}{(\kappa^2 + \tau^2)^{\frac{3}{2}}}(\kappa\hat{\mathbf{t}} - \tau\hat{\mathbf{b}}) \quad (\text{H.8})$$

$$= \frac{\kappa\tau_s - \kappa_s\tau}{(\kappa^2 + \tau^2)}\hat{\mathbf{x}} \quad (\text{H.9})$$

In a similar fashion it can be shown that:

$$\hat{\mathbf{x}}_s = -\frac{\kappa\tau_s - \kappa_s\tau}{(\kappa^2 + \tau^2)}\hat{\mathbf{z}} + (\kappa^2 + \tau^2)^{\frac{1}{2}}\hat{\mathbf{n}} \quad (\text{H.10})$$

$$\hat{\mathbf{n}}_s = -(\kappa^2 + \tau^2)^{\frac{1}{2}}\hat{\mathbf{x}} \quad (\text{H.11})$$

So, we have arrived at a new F-S description that describes the position of the helix axis rather than the backbone of the filament. In this new description, we can define a new curvature that describes how the helix axis is bent by  $\mathcal{K} = \kappa\tau_s - \kappa_s\tau/(\kappa^2 + \tau^2)$  and a new torsion  $\mathcal{T} = (\kappa^2 + \tau^2)^{\frac{1}{2}}$ . Our new equations can be rewritten in F-S form as:

$$\hat{\mathbf{z}}_s = \mathcal{K}\hat{\mathbf{x}} \quad (\text{H.12})$$

$$\hat{\mathbf{x}}_s = -\mathcal{K}\hat{\mathbf{z}} + \mathcal{T}\hat{\mathbf{n}} \quad (\text{H.13})$$

$$\hat{\mathbf{n}}_s = -\mathcal{T}\hat{\mathbf{x}} \quad (\text{H.14})$$

It is clear that  $\mathcal{K} = 0$  when  $\kappa$  and  $\tau$  are constant. This implies that  $\hat{\mathbf{z}}$  only rotates when  $\kappa_s \neq 0$  or  $\tau_s \neq 0$ . In other words, the helix axis remains straight unless the curvature or torsion are changing.

To describe the block angle that is seen in flagella when two helices of differing torsion are joined, we define  $\hat{\mathbf{z}}_0$  to be the direction of the helix axis at one end of the flagella. The angle between this axis and the helix axis at any other point along the flagella is then given by  $\cos(\alpha(s)) = \hat{\mathbf{z}}_0 \cdot \hat{\mathbf{z}}(s)$ . Taking a spatial derivative yields an equation that describes how this angle varies along the filament.

$$-\alpha_s \sin \alpha = \hat{\mathbf{z}}_0 \cdot \hat{\mathbf{z}}_s \quad (\text{H.15})$$

$$= \mathcal{K} \hat{\mathbf{z}}_0 \cdot \hat{\mathbf{x}} \quad (\text{H.16})$$

$$= \mathcal{K} \sin \alpha \cos \theta \quad (\text{H.17})$$

where  $\theta$  is the angle through which  $\hat{\mathbf{x}}$  rotates into  $\hat{\mathbf{n}}$ . This gives

$$\alpha_s = -\mathcal{K} \cos \theta. \quad (\text{H.18})$$

If we assume that the junction width between the two helices is zero, then  $\hat{\mathbf{x}}$  will not rotate into  $\hat{\mathbf{n}}$  at all as we pass from one helix to the next. In this case,  $\alpha_s = -\mathcal{K}$ . Writing this out explicitly:

$$\alpha = -\int_0^L \frac{\kappa \tau_s - \kappa_s \tau}{(\kappa^2 + \tau^2)} ds \quad (\text{H.19})$$

In our simplest picture of bistable helices, the curvature remains constant and the torsion changes. Therefore,

$$\alpha = -\int_0^L \frac{\kappa \tau_s}{(\kappa^2 + \tau^2)} ds \quad (\text{H.20})$$

$$= -\int_{\tau(0)}^{\tau(L)} \frac{\kappa d\tau}{(\kappa^2 + \tau^2)} \quad (\text{H.21})$$

$$= \tan^{-1}(\tau_+/\kappa) - \tan^{-1}(\tau_-/\kappa) \quad (\text{H.22})$$

giving the block angle for a front of zero width, with  $\tau_+ = \tau(0)$  and  $\tau_- = \tau(L)$ . However, if we would like to calculate the correction to this, then we need to expand (H.18), in terms of  $\theta$ . The first correction to the block angle comes from

$$\alpha \simeq -\int_0^L \mathcal{K} \left(1 - \frac{\theta^2}{2}\right) ds \quad (\text{H.23})$$

$$\simeq \alpha_0 + \int_0^L \frac{\mathcal{K} \theta^2}{2} ds \quad (\text{H.24})$$

Since  $\theta$  is the angle that  $\hat{\mathbf{x}}$  rotates into  $\hat{\mathbf{n}}$ , when there is a zero front width, this can be found from  $-\theta_s \sin \theta = \hat{\mathbf{x}}_0 \cdot \hat{\mathbf{x}} = \mathcal{T} \sin \theta$ , and, therefore,

$$\theta \simeq - \int_0^s \mathcal{T} ds' \quad (\text{H.25})$$

$$\simeq - \int_0^s (\kappa^2 + \tau^2)^{\frac{1}{2}} ds' \quad (\text{H.26})$$

$$\simeq (\kappa^2 + \tau^2)^{\frac{1}{2}} s \quad (\text{H.27})$$

Plugging this into (H.24) gives

$$\alpha - \alpha_0 \simeq \int_0^L s \kappa \tau_s ds \quad (\text{H.28})$$

where it has, once again, been used that  $\kappa_s = 0$ . We can solve this equation by noting that a bistable twist potential gives a front with a torsional shape that is given by  $\tau = \tau_+ \tanh(s/2\xi)$  where  $\xi$  is a parameter that fixes the front width. With this form for  $\tau$ ,  $\tau_s = (\tau_+/2\xi)/\cosh^2(s/2\xi)$ . Since this function is sharply peaked at zero, we can take our integration limits out to  $\pm\infty$  and set  $\tau_+ = \tau(-\infty)$  and  $\tau_- = \tau(\infty)$ . This leads to the equation

$$\alpha - \alpha_0 \simeq \frac{\kappa \tau_+}{2\xi} \int_{-\infty}^{\infty} \frac{s^2 ds}{\cosh^2(s/2\xi)} \quad (\text{H.29})$$

$$\simeq 2\kappa \tau_+ \xi^2 \Gamma(3) \zeta(2) \quad (\text{H.30})$$

$$\simeq (2\pi^2/3) \kappa \tau_+ \xi^2 \quad (\text{H.31})$$

A numerical integration of the basis vectors with the given torsion was done and shows good agreement with this equation at small values of  $\xi$  (See Fig. H.1).

These calculations, so far, have all been done within in the F-S frame. Though using the F-S frame has become fairly standard, it is more natural to use the material frame to describe the shape of a filament. To extend these calculations over to the material frame, we redefine the basis vectors as

$$\hat{\mathbf{z}} = \boldsymbol{\Omega}/|\boldsymbol{\Omega}| \quad (\text{H.32})$$

$$\hat{\mathbf{n}} = (\Omega_2 \hat{\mathbf{e}}_1 - \Omega_1 \hat{\mathbf{e}}_2)/(\Omega_1^2 + \Omega_2^2)^{\frac{1}{2}} \quad (\text{H.33})$$

$$\hat{\mathbf{x}} = \left( \Omega_3 (\Omega_1 \hat{\mathbf{e}}_1 + \Omega_2 \hat{\mathbf{e}}_2) - (\Omega_1^2 + \Omega_2^2) \hat{\mathbf{e}}_3 \right) / |\boldsymbol{\Omega}| (\Omega_1^2 + \Omega_2^2)^{\frac{1}{2}} \quad (\text{H.34})$$

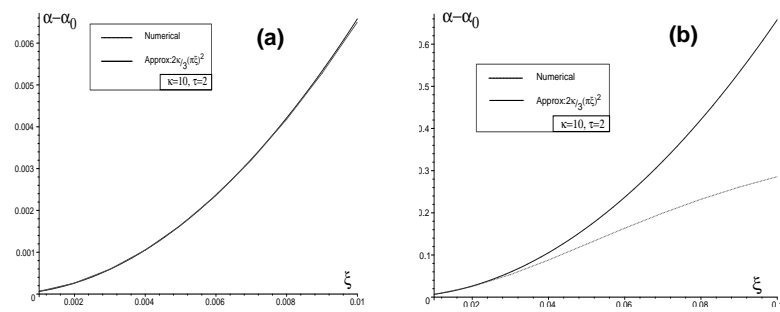


Figure H.1: (a) Numerical and Analytic results for the deviation in the block angle due to a finite width front. (b) shows the deviation that occurs at large  $\xi$ . Figure courtesy of A. Goriely.

## Appendix I

### Bistable Parameters - From Hotani's data

If we assume a bistable potential, we can derive the parameters that go into the twist energy functional from Hotani's data [11]. Hotani observed that the pitch and radius of the normal state of flagella was  $2.3\mu\text{m}$  and  $0.23\mu\text{m}$ , respectively. He also observed that the semi-coiled state had a pitch and radius of  $1.24\mu\text{m}$  and  $0.26\mu\text{m}$ , respectively. This corresponds to a twist density of  $1.96\mu\text{m}^{-1}$  for the normal state and  $1.84\mu\text{m}^{-1}$  for the semi-coiled. It was also observed that it required a torque of roughly  $1 \times 10^{-12}\text{erg}$  to induce the transition from normal to semi-coiled. Assuming a twist energy functional of:

$$\mathcal{E} = \int \left( \frac{a}{2}\Omega^2 + \frac{b}{3}\Omega^3 + \frac{c}{4}\Omega^4 + \frac{\gamma}{2}\Omega_s^2 \right) ds \quad (\text{I.1})$$

the first three parameters  $a$ ,  $b$ , and  $c$  can be approximated as:

$$c = \frac{12.0V_b}{\Omega_+^3(10\Omega_+ - \Omega_-)} \quad (\text{I.2})$$

$$b = -c(\Omega_+ + \Omega_-) \quad (\text{I.3})$$

$$a = \Omega_+\Omega_-c \quad (\text{I.4})$$

where  $\Omega_+$  is the twist density for the normal state,  $\Omega_-$  is the twist density for the semi-coiled state, and  $V_b$  is the energy barrier for the normal state. Approximating the energy barrier as  $V_b = \tau\Omega_+$ , where  $\tau$  is the torque required to cause the transition, we can solve for these parameters, with  $V_b \approx 10^{-7}\text{erg/cm}$ , gives  $c = 7.4 \times 10^{-25}\text{erg}\cdot\text{cm}^3$ ,  $b = -8.8 \times 10^{-22}\text{erg}\cdot\text{cm}^2$ , and  $a = -2.7 \times 10^{-16}\text{erg}\cdot\text{cm}$ .

From this information and the upper bound that we set on the front width,  $\xi$ , we can estimate the last parameter,  $\gamma = (2a)^{\frac{1}{2}}\xi = 1.9 \times 10^{-13}\text{erg}^{\frac{1}{2}}\cdot\text{cm}^{\frac{3}{2}}$ , with  $\xi \simeq 80\text{nm}$ .

Hotani's data actually gives four values to fit,  $\Omega_+$ ,  $\Omega_-$ ,  $V_b$ , and  $\Delta V$  the potential difference between the  $\Omega_+$  state and the  $\Omega_-$  state. The above mentioned parameters underestimate the observed  $\Delta V$  by about an order of magnitude. Therefore, a more realistic twist potential may involve a linear piece as well,

$$\mathcal{E} = \int \left( d\Omega + \frac{a}{2}\Omega^2 + \frac{b}{3}\Omega^3 + \frac{c}{4}\Omega^4 + \frac{\gamma}{2}\Omega_s^2 \right) ds . \quad (\text{I.5})$$

## Appendix J

### Stretching a Bistable Helix

To begin to make predictions for how a bistable helix is different than a normal one, the simplest problem that can be addressed is that of stretching a spring that has a bistable potential in the twist. We start with the moment and force equations for a bistable helix,

$$\mathbf{M} = A \left[ (\Omega_1 - \Omega_1^0) \hat{\mathbf{e}}_1 + (\Omega_2 - \Omega_2^0) \hat{\mathbf{e}}_2 \right] + \left( \frac{\delta \mathcal{E}}{\delta \Omega_3} \right) \hat{\mathbf{e}}_3 \quad (\text{J.1})$$

$$\mathbf{M}_s = -\hat{\mathbf{e}}_3 \times \mathbf{F} \quad (\text{J.2})$$

If we want to examine the extension that occurs when a bistable helix is under a tension,  $\mathbf{F}$ , directed along its axis, we can use the result that the axis of the helix is given by  $\hat{\mathbf{z}} = \boldsymbol{\Omega}/|\boldsymbol{\Omega}|$ . This gives that:

$$\mathbf{M}_s = \left[ \frac{\Omega_2 \hat{\mathbf{e}}_1 - \Omega_1 \hat{\mathbf{e}}_2}{|\boldsymbol{\Omega}|} \right] F \quad (\text{J.3})$$

where  $\mathbf{F} = F\hat{\mathbf{z}}$ . Combining this with Eq. 2, gives three coupled ODE's:

$$A \left[ \Omega_{1,s} - \Omega_3(\Omega_2 - \Omega_2^0) \right] + \Omega_2 \left( \frac{\delta \mathcal{E}}{\delta \Omega_3} \right) = \left( \frac{\Omega_2}{|\boldsymbol{\Omega}|} \right) F \quad (\text{J.4})$$

$$A \left[ \Omega_{2,s} + \Omega_3(\Omega_1 - \Omega_1^0) \right] - \Omega_1 \left( \frac{\delta \mathcal{E}}{\delta \Omega_3} \right) = - \left( \frac{\Omega_1}{|\boldsymbol{\Omega}|} \right) F \quad (\text{J.5})$$

$$\left( \frac{\delta \mathcal{E}}{\delta \Omega_3} \right)_s + A \left[ \Omega_2 \Omega_1^0 - \Omega_1 \Omega_2^0 \right] = 0 \quad (\text{J.6})$$

Switching to the complex notation,  $\psi = \Omega_1 + i\Omega_2$  and  $\psi^0 = \Omega_1^0 + i\Omega_2^0$ :

$$A \left[ \psi_s + i\Omega_3(\psi - \psi^0) \right] = i\psi \left[ \left( \frac{\delta \mathcal{E}}{\delta \Omega_3} \right) - \left( \frac{F}{(|\psi|^2 + \Omega_3^2)^{\frac{1}{2}}} \right) \right] \quad (\text{J.7})$$

$$\left( \frac{\delta \mathcal{E}}{\delta \Omega_3} \right)_s = \frac{A}{2} \mathcal{I}m(\psi \psi^{0*}) \quad (\text{J.8})$$

If we deform the spring in such a way as to create a new helix with different pitch and radius, then  $\psi_s = 0$ , and:

$$A\Omega_3(\psi - \psi^0) = \psi \left[ \left( \frac{\delta\mathcal{E}}{\delta\Omega_3} \right) - \left( \frac{F}{(|\psi|^2 + \Omega_3^2)^{\frac{1}{2}}} \right) \right] \quad (\text{J.9})$$

To find how much the spring is stretched, we need a geometrical relation between  $\psi$ ,  $\Omega_3$ , and the distance that the spring is stretched. This we can derive from the assumption that we have a helix. This implies that  $\Omega_3$  is constant, or  $(\delta\mathcal{E}/\delta\Omega_3)_s = 0$ . Also, if we define the total contour length of the helix as  $L_t$ , the actual length along the axis as  $L$ , and the unstretched axial length as  $L_0$ , then we can use the fact that for one turn the contour length is  $\ell = 2\pi/(|\psi|^2 + \Omega_3^2)^{\frac{1}{2}}$  and the axial distance is  $\ell_{\perp} = 2\pi\Omega_3/(|\psi|^2 + \Omega_3^2)$ . This implies that the number of turns,  $N$ , which remains constant as long as there are no induced chirality inversions, is given by  $N = L_t/\ell$  and  $L = N\ell_{\perp}$ . This also implies that:

$$\Omega_3^2 = (2\pi N/L_t)^2 - |\psi|^2 \quad (\text{J.10})$$

and therefore:

$$L = \frac{L_t^2 \left( (2\pi N/L_t)^2 - |\psi|^2 \right)^{\frac{1}{2}}}{2\pi N} \quad (\text{J.11})$$

$$= L_t \left( 1 - \left( \frac{\kappa L_t}{2\pi N} \right)^2 \right)^{\frac{1}{2}} \quad (\text{J.12})$$

where  $\kappa = |\psi|$ . And therefore:

$$|\psi|^2 = \left( \frac{2\pi N}{L_t} \right)^2 \left( 1 - (L/L_t)^2 \right) \quad (\text{J.13})$$

$$\Omega_3 = \frac{2\pi N L}{L_t^2} \quad (\text{J.14})$$

This gives that:

$$A \left( (2\pi N/L_t)^2 - |\psi|^2 \right)^{\frac{1}{2}} (\psi - \psi^0) = \psi \left( \left( \frac{\delta\mathcal{E}}{\delta\Omega_3} \right) - \frac{F L_t}{2\pi N} \right) \quad (\text{J.15})$$

or:

$$\left( \frac{2\pi N A}{L_t} \right) (L/L_t) \frac{(\psi - \psi^0)}{\psi} = \left( \left( \frac{\delta\mathcal{E}}{\delta\Omega_3} \right) - \frac{F L_t}{2\pi N} \right) \quad (\text{J.16})$$

$$\left( \frac{2\pi N A L}{L_t^2} \right) \left( 1 - \left( \frac{L_t^2 - L_0^2}{L_t^2 - L^2} \right)^{\frac{1}{2}} \right) = \left( \left( \frac{\delta\mathcal{E}}{\delta\Omega_3} \right) - \frac{F L_t}{2\pi N} \right) \quad (\text{J.17})$$

### Normal Spring

For a normal spring,  $(\delta\mathcal{E}/\delta\Omega_3) = C(\Omega_3 - \Omega_3^0)$ . This gives that:

$$\left(\frac{2\pi NAL}{L_t^2}\right) \left(1 - \left(\frac{L_t^2 - L_0^2}{L_t^2 - L^2}\right)^{\frac{1}{2}}\right) = C(\Omega_3 - \Omega_3^0) - \frac{FL_t}{2\pi N} \quad (\text{J.18})$$

or:

$$1 - \left(\frac{L_t^2 - L_0^2}{L_t^2 - L^2}\right)^{\frac{1}{2}} = \frac{\Gamma(L - L_0)}{L} - \frac{\tilde{F}L_t}{4\pi^2 N^2 L} \quad (\text{J.19})$$

where  $\Gamma = C/A$  and  $\tilde{F} = FL_t^3/A$ . This equation is the same as what has previously been derived [39].

### Bistable Spring

If we assume a bistable twist potential,  $V(\Omega) = a/2\Omega^2 + b/3\Omega^3 + c/4\Omega^4$  (where the 3 has been dropped for convenience), this changes the extension equation as:

$$\left(\frac{2\pi NAL}{L_t^2}\right) \left(1 - \left(\frac{L_t^2 - L_0^2}{L_t^2 - L^2}\right)^{\frac{1}{2}}\right) = \Omega(a + b\Omega + c\Omega^2) - \frac{FL_t}{2\pi N} \quad (\text{J.20})$$

or:

$$1 - \left(\frac{L_t^2 - L_0^2}{L_t^2 - L^2}\right)^{\frac{1}{2}} = \tilde{a} + \tilde{b} \left(\frac{2\pi NL}{L_t^2}\right) + \tilde{c} \left(\frac{2\pi NL}{L_t^2}\right)^2 - \frac{\tilde{F}L_t}{4\pi^2 N^2 L} \quad (\text{J.21})$$

where  $\tilde{x} = x/A$ , and  $\tilde{F} = FL_t^3/A$ .



## Appendix K

### Fiber Dynamics with an Attached Bead

The drag per length on a fiber goes as  $f_d = \zeta_{\perp} v$  where  $\zeta_{\perp} = 4\pi\eta/(\ln(L/2a) + \frac{1}{2})$  is the drag coefficient of a filament of radius  $a$  as calculated by slender body hydrodynamics. The drag on a bead moving at velocity  $v$  is  $F_d = \zeta_b v$  where  $\zeta_b = 6\pi\eta R$  with  $R$  the radius of the bead. Therefore, the ratio of the drag of the fiber to that of the bead is approximately:

$$\frac{F_d}{f_d L} = \epsilon \approx \frac{3R}{2L} \left[ \ln(L/2a) + \frac{1}{2} \right] \quad (\text{K.1})$$

For a bead of radius  $1\mu\text{m}$  and a fiber of length  $30\mu\text{m}$ , this gives that  $F_d/f_d L \approx 0.16$ , which implies that the drag on the bead is not negligible compared with that on the fiber. This means that we should take the force of the bead into account when doing calculations. This can be done straightforwardly. The boundary conditions at the clamped end remain the same,  $y(0) = y_x(0) = 0$ . The bead end remains torqueless,  $y_{xx}(L) = 0$ , but there is now a force at the end, which implies  $Ay_{3x}(L) = F_d$ . These boundary conditions are written out under the assumption that there is a small amplitude displacement. The equation of motion for this displacement is:

$$\zeta_{\perp} y_t = -Ay_{4x} \quad (\text{K.2})$$

From this we can rewrite the force boundary condition as:  $y_{3x}(L) = -(\zeta_b/\zeta_{\perp})y_{4x}(L)$ . Using biharmonic functions for  $y$  and the free end boundary conditions gives:

$$y(x) = a(\cos(kx) - \cosh(kx)) + b(\sin(kx) - \sinh(kx)) \quad (\text{K.3})$$

and the last two boundary conditions can be written as:

$$a(\cos(kL) + \cosh(kL)) + b(\sin(kL) + \sinh(kL)) = 0 \quad (\text{K.4})$$

$$(a + b\epsilon kL) (\sin(kL) - \sinh(kL)) = (b - a\epsilon kL) \cos(kL) + (b + a\epsilon kL) \cosh(kL) \quad (\text{K.5})$$

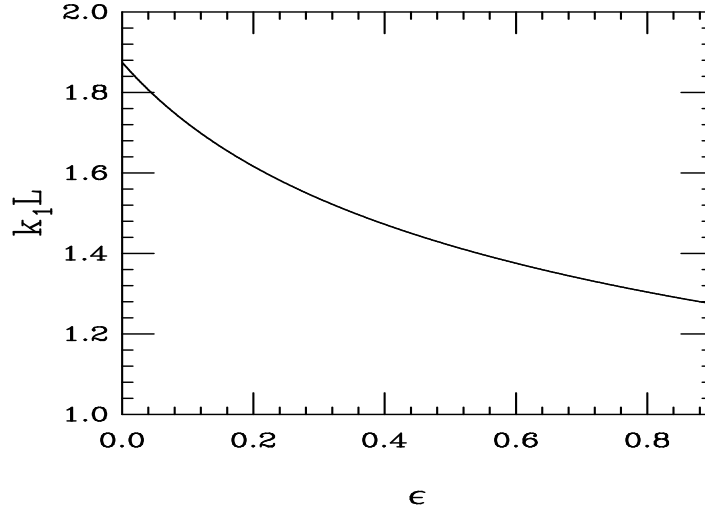


Figure K.1: Variation in  $k_1 L$ , where  $k_1$  is the wavenumber of the first mode, with  $\epsilon$ .

These equations lead to a solvability condition on  $k$  of:

$$1 + \cos(kL) \cosh(kL) = \epsilon k L (\cosh(kL) \sin(kL) - \cos(kL) \sinh(kL)) \quad (\text{K.6})$$

Therefore, the new problem of calculating the bending modulus,  $A$ , from the relaxation time, boils down to solving the above equation for  $k$ , since we can separate the dynamic equation by parts,  $y(x, t)/y_0 = f(x)T(t)$ , where  $f(x)$  are the above biharmonic functions normalized to an end amplitude of 1, which gives:

$$T(t) \sim e^{-(Ak^4/\zeta_\perp)t} \quad (\text{K.7})$$

In other words, it is expected that a fiber, in a viscous fluid, that is bent slightly will relax back to its unstressed state with a characteristic decay time given by:

$$\tau = \frac{\zeta_\perp}{Ak_1^4}, \quad (\text{K.8})$$

where  $k_1$  is the first (smallest) wave number found from the solution of the transcendental equation (K.6).

## REFERENCES

- [1] C.W. Wolgemuth, T.R. Powers, and R.E. Goldstein. Twirling and whirling: Viscous dynamics of rotating elastic filaments. *Phys. Rev. Lett.* **84**, 1623 (2000).
- [2] R. E. Goldstein, A. Goriely, G. Huber, and C. W. Wolgemuth. Bistable helices. *Phys. Rev. Lett.* **84**, 1631 (2000).
- [3] N.H. Mendelson, J.E. Sarlls, C.W. Wolgemuth, and R.E. Goldstein. Chiral self-propulsion of growing bacterial macrofibers on a solid surface. *Phys. Rev. Lett.* **84**, 1627 (2000).
- [4] G. Kirchhoff, *Vorlesungen über mathematische Physik* (B. G. Teubner, Leipzig, 1883).
- [5] L.F. Liu and J.C. Wang. Supercoiling of the DNA template during transcription. *Proc. Natl. Acad. Sci. U.S.A.* **84**, 7024 (1987).
- [6] H.-Y. Wu, S.H. Shuy, J.C. Wang, and L.F. Liu. Transcription generates positively and negatively supercoiled domains in the template. *Cell* **53**, 433 (1988).
- [7] J.F. Marko. DNA under high tension: overstretching, undertwisting, and relaxation dynamics. *Phys. Rev. E.* **57**, 2134 (1998).
- [8] R.M. Macnab and M.K. Ornston. Normal-to-curly transitions and their role in bacterial tumbling. Stabilization of an alternative quarternary structure by mechanical force. *J. Mol. Biol.* **112**, 1 (1977).
- [9] K. A. Fahrner, S. M. Block, S. Krishnaswamy, J. S. Parkinson, and H. C. Berg. A mutant hook-associated protein (HAP3) facilitates torsionally induced transformations of the flagellar filament of *Escherichia Coli*. *J. Mol. Biol.* **238**, 173 (1994).
- [10] K. Namba and F. Vonderviszt. Molecular architecture of bacterial flagella. *Quart. Rev. Biophys.* **30**, 1 (1997).
- [11] H. Hotani. Micro-video study of moving bacterial filaments. *J. Mol. Biol.* **156**, 791 (1982).
- [12] C.H. Wiggins, D. Riveline, R.E. Goldstein, and A. Ott. Trapping and wiggling: Elastohydrodynamics of driven microfilaments. *Biophys. J.* **74**, 1043 (1998).
- [13] G.G. Stokes, *Trans. Cambridge Philos. Soc.* **9**, 8 (1851).

- [14] J. Keller and S. Rubinow. Slender body theory for slow viscous flow. *J. Fluid Mech.* **44**, 705 (1976).
- [15] N.H. Mendelson. Helical growth of *Bacillus subtilis*: A new model of cell growth. *Proc. Natl. Acad. Sci. U.S.A.* **73**, 1740 (1976).
- [16] N. H. Mendelson. Self-assembly of bacterial macrofibers: A system based on hierarchies of helices. *Mat. Res. Soc. Symp. Proc.* **255**, 43 (1992).
- [17] N. H. Mendelson, J. J. Thwaites, J. O. Kessler, and C. Li. Mechanics of bacterial macrofiber initiation. *J. Bacteriol.* **177**, 7060 (1995).
- [18] M.J. Tilby. Helical shape and wall synthesis in a bacterium. *Nature* **266**, 450 (1977).
- [19] N. H. Mendelson, D. Favre, and J. J. Thwaites. Twisted states of *Bacillus subtilis* macrofibers reflect structural states of the cell wall. *Proc. Natl. Acad. Sci. USA* **81**, 3562 (1984).
- [20] N. H. Mendelson and D. Favre. Regulation of *Bacillus subtilis* macrofiber twist development by ions: Effects of magnesium and ammonium. *J. Bacteriol.* **169**, 519 (1987).
- [21] N. H. Mendelson. Regulation of *Bacillus subtilis* macrofiber twist development by D-Cycloserine. *J. Bacteriol.* **170**, 2336 (1988).
- [22] C.R. Calladine. Construction of bacterial flagella. *Nature* **255**, 121 (1975).
- [23] C.R. Calladine. Change of waveform in bacterial flagella: The role of mechanics at the molecular level. *J. Mol. Biol.* **118**, 457 (1978).
- [24] S. Asakura. Polymerization of flagellin and polymorphism of flagella. *Adv. Biophys. (Japan)* **1**, 99 (1970).
- [25] H. Hotani. Light microscope study of mixed helices in reconstituted *Salmonella* flagella. *J. Mol. Biol.* **106**, 151 (1976).
- [26] S. Asakura and T. Iino. Polymorphism of *Salmonella* flagella as investigated by means of *in vitro* copolymerization of flagellins derived from various strains. *J. Mol. Biol.* **64**, 251 (1972).
- [27] R. Kamiya and S. Asakura. Helical transformations of *Salmonella* flagella *in vitro*. *J. Mol. Biol.* **106**, 167 (1976).
- [28] C. Levinthal, H.R. Crane. On the unwinding of DNA. *Proc. N.A.S.* **42**, 436 (1956).
- [29] P. Nelson. Transport of torsional stress in DNA. *Proc. Natl. Acad. Sci. U.S.A.* **96**, 14342 (1999).
- [30] I. Yamashita, *et al.* Structure and switching of bacterial flagellar filaments studied by X-ray fiber diffraction. *Nature (London)* **5**, 125 (1998).

- [31] D.L. Caspar. Bacterial flagellar coiling explained by slip-and-click strand switching. *Nature (London)* **5**, 92 (1998).
- [32] H.C. Berg and R.A. Anderson. Bacteria swim by rotating their flagellar filaments. *Nature* **245**, 380 (1973).
- [33] C.H. Wiggins and R.E. Goldstein. Flexive and propulsive dynamics of elastica at low Reynolds number. *Phys. Rev. Lett.* **80**, 3879 (1998).
- [34] S. Camalet, F. Jülicher, J. Prost. Self-organized beating and swimming of internally driven filaments. *Phys. Rev. Lett.* **82**, 1590 (1999).
- [35] I. Klapper and M. Tabor. A new twist in the kinematics and dynamics of thin filaments and ribbons. *J. Phys. A: Math. Gen.* **27**, 4919 (1994).
- [36] I. Klapper. Biological applications of the dynamics of twisted rods. *J. Comp. Phys.* **125**, 325 (1996).
- [37] R.D. Kamien. Local Writhing Dynamics. *Eur. Phys. J. B* **1**, 1 (1998).
- [38] R.E. Goldstein, T.R. Powers, C.H. Wiggins. Viscous nonlinear dynamics of twist and writhe. *Phys. Rev. Lett.* **80**, 5232 (1998).
- [39] A.E.H. Love, *A Treatise on the Mathematical Theory of Elasticity*, 4th ed. (Dover Publications, New York, 1944).
- [40] S.S. Antman. Nonlinear eigenvalue problems for the whirling of heavy elastic strings. *Proc. Roy. Soc. Edin. Sec. A* **85**, 59 (1980).
- [41] A. Goriely, M. Tabor. Nonlinear dynamics of filaments: I. Dynamical Instabilities. *Physica D* **105**, 20, 44 (1997).
- [42] A. Goriely, M. Tabor. Nonlinear dynamics of filaments: II. Instabilities of helical rods. *Proc. Soc. Lond. A Mat.* **453**, 2583 (1997).
- [43] A. Goriely, M. Tabor. *Proc. Soc. Lond. A Mat.* **454**, 3183 (1998).
- [44] J.J. Thwaites and N.H. Mendelson. Mechanical properties of peptidoglycan as determined from bacterial thread. *Int. J. Biol. Macromol.* **11**, 201 (1989).
- [45] M.C. Cross and P.C. Hohenberg. Pattern formation outside of equilibrium. *Rev. Mod. Phys.* **65**, 851 (1993).
- [46] W.H. Press, W.T. Vetterling, S.A. Teukolsky, and B.P. Flannery, *Numerical Recipes in C*, 2nd ed. (Cambridge University Press, 1992), Ch. X.
- [47] R.E. Goldstein, D.J. Muraki, D.M. Petrich. Interface proliferation and the growth of labyrinths in a reaction-diffusion system. *Phys. Rev. E.* **53**, 3933 (1996).
- [48] G.I. Taylor. Analysis of the swimming of microscopic organisms. *Proc. Roy. Soc. A* **211**, 225 (1952).

- [49] E. M. Purcell. Life at low Reynolds number. *Am. J. Phys.* **45**, 3 (1977).
- [50] D. Coombs, G. Huber, R.E. Goldstein, and J.O. Kessler. (to be published).
- [51] S. Wölfl, B. Wittig and A. Rich. Identification of transcriptionally induced Z-DNA segments in the human c-myc gene. *Biochim. Biophys. Acta* **1264**, 294 (1995).
- [52] V. Müller *et al.* Z-DNA forming sites within the human beta-globin gene cluster. *Proc. Natl. Acad. Sci. USA* **93**, 780 (1996).
- [53] A. Rich and A. Herbert. The biology of left-handed Z-DNA. *J. Biol. Chem.* **271**, 11595 (1996).
- [54] A. Rich. DNA comes in many forms. *Gene* **135**, 99 (1993).
- [55] A. Wang *et al.* Left-handed double helical DNA: Variations in the backbone conformation. *Science* **211**, 171 (1981).
- [56] A. Goriely *et al.*, preprint (1999).
- [57] Helices can also arise from symmetry-breaking instabilities where twist does not play a role; see V. Frette *et al.*. Coiling of cylindrical membrane stacks with anchored polymers. *Phys. Rev. Lett.* **83**, 2465 (1999).
- [58] A. Goriely and M. Tabor. Spontaneous helix hand reversal and tendril perversion in climbing plants. *Phys. Rev. Lett.* **80**, 1564 (1998).
- [59] J.F. Marko and E.D. Siggia. Bending and twisting elasticity of DNA. *Macromolecules.* **27**, 981 (1994).
- [60] J.F. Marko and E.D. Siggia. Bending and twisting elasticity of DNA. *Macromolecules.* **29** (1996) 4820.
- [61] R.E. Goldstein and S.A. Langer. Nonlinear dynamics of stiff polymers. *Phys. Rev. Lett.* **75**, 1094 (1995).
- [62] K. Nakayama, H. Segur, and M. Wadati. Integrability and the motion of curves. *Phys. Rev. Lett.* **69**, 2603 (1992).
- [63] A. Goriely and M. Tabor. New amplitude equations for thin elastic rods. *Phys. Rev. Lett.* **77**, 3537, (1996).
- [64] Others have proposed nonlinear elastic models based on expansions in powers of  $\kappa$  and the torsion  $\tau$  [e.g. W. Helfrich. Helical bilayer structures due to spontaneous torsion of the edges. *J. Chem. Phys.* **85**, 1085 (1986)], but these can be problematic due to singularities in  $\tau$  at inflection points.
- [65] E. H. Dill. Kirchoff theory of rods. *Arch. Hist. Exact. Sci.* **44**, 2 (1992).
- [66] S. S. Antman, *Nonlinear problems of elasticity* (Springer Verlag, New York 1995).

- [67] Since the two minima are locally stable there is no velocity-selection problem like that found in the invasion of a stable state into an unstable one.
- [68] J.W. Cahn and J.E. Hilliard. *J. Chem. Phys.* **28**, 258 (1958).
- [69] P.C. Hohenberg and B. I. Halperin. Theory of dynamics critical phenomena. *Rev. Mod. Phys.* **49**, 435 (1977).
- [70] W. van Saarloos and P.C. Hohenberg. Fronts, pulses, sources and sinks in generalized complex Ginzburg-Landau equations. *Physica D* **56**, 303 (1992).
- [71] Pijper and Abraham. *J. Gen. Microbiol.* **10**, 452 (1954).
- [72] N. H. Mendelson. Helical *Bacillus subtilis* macrofibers: Morphogenesis of a bacterial macroorganism. *Proc. Natl. Acad. Sci. U.S.A.* **75**, 2478 (1978).
- [73] N. H. Mendelson and J. J. Thwaites. *Mat. Res. Soc. Symp. Proc.* **174**, 171 (1990).
- [74] S. Childress. *Swimming and Flying in Nature*. (Cambridge, Cambridge University Press, 1981).
- [75] N.H. Mendelson. Dynamics of *Bacillus subtilis* helical macrofiber morphogenesis: writhing, folding, close packing, and contraction. *J. Bacteriol.* **151**, 438 (1982).
- [76] D. Favre, N.H. Mendelson, and J.J. Thwaites. Relaxation motions induced in *Bacillus subtilis* macrofibers by cleavage of peptidoglycan. *J. Gen. Microbiol.* **132**, 2377 (1986).
- [77] M. Tabor and I. Klapper. in *Mathematical Approaches to Biomolecular Structure and Dynamics* IMA **82**, ed. J.P. Mesirov, K. Schulten, and D. W. Sumners (Springer-Verlag, New York, 1995).
- [78] A. Zaritsky and N.H. Mendelson. Helical macrofiber formation in *Bacillus subtilis*: Inhibition by Penicillin G. *J. Bacteriol.* **158**, 1182 (1984).
- [79] A.L. Koch, *J. Theor. Biol.* **141**, 391 (1989); A.L. Koch, *Bacterial Growth and Form* (Chapman & Hall, New York, 1995).
- [80] F.B. Fuller. Decomposition of linking number of a closed ribbon: Problem from Molecular Biology. *Proc. Natl. Acad. Sci. USA* **75**, 3557 (1978).
- [81] N.R. Cozzarelli, T.C. Boles, and J. White, in *DNA Topology and its Biological Effects*, ed. by N.R. Cozzarelli and J.C. Wang (Cold Spring Harbor Laboratory, Cold Spring Harbor, NY, 1990).
- [82] C.R. Calladine and H.R. Drew. *Understanding DNA. The Molecule & How It Works* (Academic Press, New York, 1992).
- [83] J.F. Marko and E.D. Siggia. Fluctuations and supercoiling of DNA. *Science* **265**, 506 (1994).

- [84] J.F. Marko and E.D. Siggia. Statistical mechanics of supercoiled DNA. *Phys. Rev. E* **52**, 2912 (1995).
- [85] Movies of the processes described here can be found at [research.biology.arizona.edu/mendelson/mands](http://research.biology.arizona.edu/mendelson/mands).
- [86] TB consisted of 10 g of Bacto Tryptose (Difco), 3 g of Bacto Beef Extract (Difco), and 5 g of NaCl, each per liter of deionized water. See [20].
- [87] J. Lighthill, *Mathematical Biofluidynamics*. (Philadelphia, SIAM, 1975).
- [88] Fiber density at 24°C in TB is 1.015 g/cm<sup>3</sup> from the sedimentation velocity  $v \simeq (2/9)R^2\Delta\rho g/\eta$  of fiber-ball structures of radius  $R$  [N. H. Mendelson, B. Salhi, and C. Li, in *Bacteria as Multicellular Organisms*, J. A. Shapiro and M. Dworkin Eds., p. 339 (Oxford Univ. Press, NY, 1997)], with  $\eta$  the viscosity, and  $\Delta\rho$  the density difference, approximating the dense fiber-ball as a solid sphere.
- [89] J. J. Thwaites and N. H. Mendelson. Mechanical behavior of bacterial cell walls. *Adv. Microbiol. Physiol.* **32**, 173 (1991).
- [90] K. Svoboda and S.M. Block. Biological applications of optical forces. *Ann. Rev. Biophys. Biomol. Struct.* **23**, 247 (1994).
- [91] J. Gelles, B.J. Schnapp, and M.P. Sheetz. Tracking kinesin driven movements with nanometre-scale precision. *Nature* **331**, 450 (1988).
- [92] M. Elbaum, D.K. Fygenson, and A. Libchaber. Buckling microtubules in vesicles. *Phys. Rev. Lett.* **76**, 4078 (1996).
- [93] See *e.g.* L.D. Landau and E.M. Lifshitz, *Theory of Elasticity*, 3rd ed. (Pergamon Press, Oxford, 1986).
- [94] Due to a University of Arizona policy, the acknowledgements are limited to one page. As the people who have enabled me to reach this point are numerous, I could not fit them all in such a limited space, and so I continue, here.

Beyond just the scientists that coauthored papers with me, I would like to thank a number of other scientists at the University of Arizona who have instilled in me a great passion for physics and have also offered help along the way. I would like to thank John Kessler, Srinivas Manne, Koen Visscher, John Rutherford, and William Bickel. My undergraduate and graduate schooling would never have been complete had I not taken classes with Doug Toussaint. Thank you Doug for demanding brutal calculations that pushed my abilities as well as requiring that a person utilizes insight rather than just blindly applying mathematical formulae.

I would like to acknowledge my fellow graduate students at the University of Arizona who have engaged me in numerous conversations, both scientific and other, provided me with assistance and questions to steer me in the right direction, and found things for me to do in my spare time that have enriched my life and my intellect. Of these,



I would especially like to thank Pete Johnson, Mike Fromerth, Todd Thompson, Uli Hiller, SungKyun Park (Sparky), Tom Burch and Rob McCroskey. The latter two have not only been there for me in school, but have also joined me as I flounder through the world of music. Thank you, Rob, also, for your companionship in Advanced Lab, without which I would definitely only be a theorist now.

Finally, I would like to thank the “behind the scenes” people: my family and friends. These are the people who gave me encouragement along the way and were also there for me to take me away from the science when I needed it. First off, I will thank my friends: Eric Andreen, Bob Baker, Greg Guerin, Jonathan Wayne Mason, Dan Perovich, Matt Reick, and Brian (Woody) Woodward. And then my mom, Aloure Wolgemuth and my brother Jonathan. Lastly, my fiancée and best friend, Justine Rae Forbes (soon to be Wolgemuth) who doesn’t know what she’s in for. Without all of you, my life would not be nearly as bright, enjoyable, and down right crazy as it is.